EXPERIMENTAL STUDY OF INTENSE AND BROADBAND TERAHERTZ WAVE RADIATION BY BACKWARD WAVE OSCILLATOR

Dissertation in Electrical and Information Engineering submitted to the Graduate School of Science and Technology of Niigata University in partial fulfillment of the requirements for the degree of Doctor of Philosophy

By

Min Thu San

Graduate School of Science and Technology

Niigata University

March 2018

Abstract

In this dissertation, intense and broadband terahertz radiations by backward wave oscillator (BWO) are experimentally and numerically studied. Compact as well as tunable devices are preferable for practical use in terahertz applications. To predict the operation of the oscillator, numerical study for the dispersion relation of the slow-wave structure (SWS) is presented in the study. By the dispersion relation, the operating frequency and operation region of the oscillator can be estimated. In the experiment, cylindrical waveguides with rectangular corrugations in the wall are used as SWSs. Various lengths of SWS are employed in the study. Electron beam with energy less than 100 kV from pule power system drives disk-type cold cathode to generate annular electron beam. External magnetic field of 0.82 T is used to confine the flow of electron beam in the axial direction. Radiations are detected by horn antennas and radiated frequency is confirmed by high pass filters.

Three types of SWSs with upper cutoff frequency of 0.1, 0.35, and 0.5 THz are employed in the BWO for terahertz radiations. Major difference among them is length of the corrugation amplitude; corrugation amplitude of 0.1 THz SWS is two (four) times larger than that of 0.35 THz (0.5 THz) SWS. The former SWS has relatively flat dispersion relation and operates as a surface-wave oscillator (SWO). Radiated output power is of ~ 20 kW with radiation frequency of 0.1 THz. Due to short length of the corrugation amplitude, 0.35 THz (0.5 THz) SWS has steep dispersion relation and operates as a surface-wave resonator (SWR). Both SWRs have tunable radiation frequency bandwidth of ~ 0.1 THz, and output power is of some kW. Peak radiation frequency of 0.4 THz for the SWR (0.5 THz) is detected in the study.

To study the operation regions of the SWO (0.1 THz), SWS lengths are varied as 20-, 40-, 80-, and 120-period. By the dispersion relation, operation regions of the SWO can be predicted that the SWO operates at π-point around the beam energy of 32.5 keV, and in BWO and travelling wave tube (TWT) regions

when the beam energy is less and greater than 32.5 keV. When the length of the SWS is relatively long: 80- and 120-period, radiations are detected at the beam voltage of less and greater than 32.5 kV, and no meaningful radiation is occurred by that voltage. When the length of the SWS is short enough: 20- and 40-period, meaningful radiations are detected even around 32.5 kV. The experimental results show the SWO with short length of the SWS operates in all regions, and with long length of the SWS operates in BWO and TWT regions. To recognize the π-point operation, two numerical methods: real wave number analysis and saddle-point analysis, are studied. The numerical results show that Cherenkov instability is of an absolute instability when the SWO operates around the π-point region.

To analysis the oscillation starting conditions of the SWRs, SWSs of 40-, 60-, 80-, and 120-period for the SWR (0.35 THz), and 120-, 160-, 320-, and 400-period for the SWR (0.5 THz) are studied. Numerical studies for oscillation starting conditions: starting energy and starting current, are also presented. For both types, the experimental results of the starting current are totally different from the numerical anticipation, and the oscillation starting condition could not be explained by the starting current condition. For the SWR (0.35 THz), the experimental results of the starting energy are decreased increasing the length of the SWS and cathode diameter, and in a good agreement with the numerical results. For the SWR (0.5 THz), the experimental results of the starting energy agree with the numerical results until when the length of the SWS is relatively short of up to 160-preiod. In the experiment, the starting energy of the SWR (0.5 THz) could not be reduced anymore when the length of the SWS is relatively long of 320-period and above.

Acknowledgment

The author would like to express his heartiest thanks and gratitude to his supervisor, Professor Kazuo Ogura, for his excellent guiding, caring, patience, responsibility, encouragement and continuous supervision. The author cannot express enough thanks to his supervisor.

The author would like to express heartfelt gratitude to Professor Kiyoyuki Yambe for his congenial support and invaluable advice throughout the research work.

The author is indebted to Professor Akira Sugawara for providing guidelines and effective suggestions in completing the research work.

The author is pleased to acknowledge all members of Experimental Group, Numerical Group and VNA Group of the laboratory for their help, patience and cooperation.

The author is particularly grateful to his father, mother, brother and sister for their noble support, encouragement and love.

Finally, special acknowledgment is due to JICA (Japan International Cooperation Agency) for providing scholarship and supporting this research work.

Contents

Chapter 1

Introduction

1.1 THz Radiation and Applications

Terahertz radiation is electromagnetic wave with frequencies of terahertz (0.1–10 THz). In the electromagnetic spectrum, terahertz radiation region is typically considered between the upper end of microwave and far-infrared region, shown in Fig. 1.1. It is also known as sub-millimeter radiation, terahertz light, terahertz wave, T-ray, T-light, T-lux and THz. Similar to microwaves, it can penetrate in wide variety of non-conducting materials such as papers, clothes, plastics, ceramic, etc. It can also penetrate in the clouds and fogs, and in addition, it is non-ionizing radiation [1]. Therefore, it has found applications in many different fields such as packaging inspection, security systems, plasma physics, radar systems, biophysics, medical and industrial imaging, nanostructure, and material science [2].

1.2 Slow-wave Devices for THz Radiation

There are many sources for terahertz radiation: thermal sources such as globar [3] and mercury lamp [4], mechanical excitation such as peeling tape [5] and surface formation [6], solid-state electronic [7], [8], lasers [9], and vacuum electronic devices [10]. Vacuum electronic devices include backward wave oscillators (BWOs) [11], surface-wave oscillators (SWOs) [12], klystrons [13],

travelling wave tubes (TWTs) [14], gyrotrons [15], free electron lasers (FELs) [16], synchrotrons [17], and Orotrons [18]. Our research works focus on the vacuum electronic devices.

Vacuum electronic devices base on the mechanism of electron beams and electromagnetic waves interaction. They can be categorized into slow-wave and fast-wave devices based on the mechanism of slow-wave and fast-wave excitation. In the slow-wave devices, the electron beams travel in straight line and interact with the electromagnetic waves which phase velocity is less than the speed of light. BWOs, TWTs, SWOs, FELs and Orotrons are of slow-wave devices. In the fast-wave devices, the electron beams travel along the curve path, and interact with the electromagnetic wave which phase velocity is larger than the speed of light. Gyrotrons and klystrons are of fast-wave devices.

The devices can be classified into O-type and M-type devices from the stand point of electron bunching in the devices. In O-type devises such as BWOs and TWTs, the electrons travel along the axial magnetic field and bunching occurs in the streaming direction. In M-type devices such as magnetrons, the electron beam moves perpendicular to the crossed electric and magnetic fields and bunching occurs in the spatial direction.

1.3 Brief History of Slow-wave Devices for THz Radiation

Slow-wave devices of BWOs, TWTs, and Orotrons or Ledatrons have been studied for higher- and moderate-power microwave sources [18]-[23], and become promising classes of intense terahertz radiation sources [24]-[30]. The devices commonly use periodically corrugated slow-wave structure (SWS). Orotrons or Ledatrons use open cavities based on the planar geometry and the slow waves cling to SWS walls. The Orotron with an open resonator and reflecting grating was first introduced in 1969 [18], and the submillimeter radiation in Orotrons was studied in

1970 at a wavelength of 0.83 mm [25]. A series of relatively powerful and high-frequency pulsed Orotorons developed has a common design and output power of 1–0.1 W in the frequency range of 90–410 GHz at a low operation voltage of up to 5 kV [26], [27].

Another realistic geometry is a cylindrical one, which has been used for high-power BWOs, TWTs and SWOs. A power level of approximately 500 MW was achieved at 8.3 GHz with a moderate voltage of approximately 500 kV using surface-wave microwave oscillator [21]. A cylindrical SWO driven with relativistic electron beam energy of 300 kV has been studied for high power radiation of megawatt level at operating frequency of 0.148 THz [12]. Since 1950s, BWOs have been used to generate microwaves up to the THz radiation. To improvement the performance of the BWOs, oversized SWSs have been employed in the BWOs. History of oversized BWOs at Niigata University is presented in Table 1.1. In the early 1940s, vacuum devices of TWTs were invented for amplification of radio frequency power [14]. A brief history of folded waveguide TWTs, gyrotron TWTs and others to date is presented in Table 1.2.

J. H. Booske summarized and presented the relation of power as a function of frequency for solid state and vacuum electronics devices [40]. Power versus frequency of compact and mobile, average power (single) devices summarized by J. H. Booske is presented in Fig. 1.2.

1.4 Motivation

For practical applications, devices operating at reduced voltage and with compact structure are preferable. Intense and/or broadband radiation devices are also desired for terahertz applications. In addition, to date BWO and TWT regions operations of an oscillator have been studied theoretically and experimentally in many research works, but not for π-point or Bragg condition operation. In this study, π-point operation as well as BWO and TWT regions operation has been

experimentally carried out with SWO (0.1 THz). Around the π-point region, the group velocity of the structure electromagnetic wave transits from TWT to BWO region and approaches zero, and absolute or convective instability could not be clearly recognized. The numerical study presented in this study pointed out that Cherenkov instability is of an absolute instability when the operation of the SWO is around the π-point region. By the electron beam with energy less than 80 keV and the external magnetic field of 0.82 T, radiated power is of some kW at THz frequency range. Tunable bandwidth of ±13% with 0.3 THz central frequency, and broadband radiation of approximately 0.1 THz with maximum frequency of 0.4 THz are experimentally carried out with SWRs in the study. Theoretically the oscillation starting energy is decreased by increasing the length of the SWS. But the experimental results showed that the starting energy saturates at some value even though the length of the SWS is changed any longer. The present study is applicable for intense, broadband and compact terahertz radiation devices.

1.5 Outline of Dissertation

This dissertation is organized as follows. Overview of the dissertation is shown in Fig. 1.3.

Chapter 1 is the introduction of the terahertz radiation. Applications of THz radiation and THz radiation sources are briefly presented. Slow-wave devices for THz radiation (vacuum electronic devices), a brief history of slow-wave devices for THz radiation, and motivation of the study are described in Section 1.2, 1.3, and 1.4, respectively.

Chapter 2 is theoretical and experimental backgrounds of the study. Theoretical background and slow-wave structure of the study are briefly presented in Section 2.2 and 2.3. Numerical study for the dispersion relation of the SWS is studied in Section 2.4. In Section 2.5, experimental background of the study is

presented. Experimental devices, slow-wave structures and cathode used in the experiment are also presented. Experimental set-up and operation are described in Section 2.6.

Chapter 3 is experimental study for terahertz radiation. Three types of SWSs with upper cutoff frequency of 0.1, 0.35, and 0.5 THz are experimentally studied. The experimental results for operating frequency and operating region of the oscillator are confirmed by the numerical study of the dispersion relation. Various lengths of SWS for each type are studied in the experiment. Intense radiation and π-point operation are obtained by the SWO (0.1 THz). Broadband radiation frequency range is recognized by the SWRs (0.35 THz) and (0.5 THz). Summary and conclusion are presented in Section 3.6.

Chapter 4 is operation of a surface-wave oscillator around π-point. The different between SWO and SWR is presented by the dispersion relation in Section 4.2. The SWS with upper cutoff frequency of 0.1 THz operates as a surface-wave oscillator. Two numerical studies of real wave number analysis and saddle-point analysis are presented in Section 4.3 and 4.4. The SWO (0.1 THz) with relatively short length of the SWS operates around the π-point. The mechanism of π-point operation is presented in Section 4.5. Summary and conclusion are presented in Section 4.6.

Chapter 5 is oscillation starting conditions of surface-wave resonators. Dispersion relation of the SWR is presented in Section 5.2. The SWSs with upper cutoff frequency of 0.35 and 0.5 THz are assumed as SWRs (0.35 THz) and (0.5 THz) due to their properties of the dispersion relations. Numerical study for oscillation starting conditions: starting energy and starting current, are presented in Section 5.3. The starting conditions obtained by experimental studies for both types are analyzed by the numerical ones in Section 5.4 and 5.5. Summary and conclusion are presented in Section 5.6.

Finally, in Chapter 6, summary of the present research work is presented.

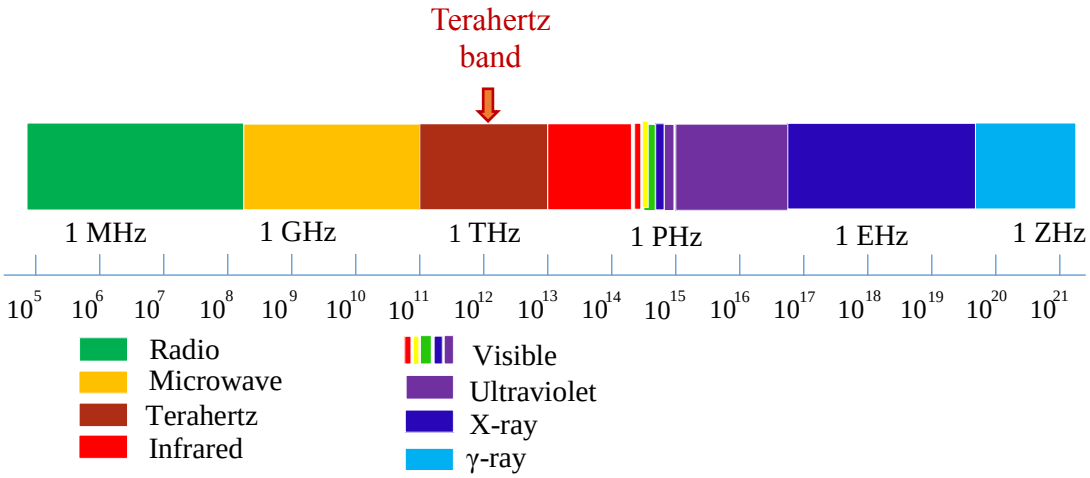

Fig. 1.1 Electromagnetic spectrum: THz radiation lies between the microwave and infrared frequencies.

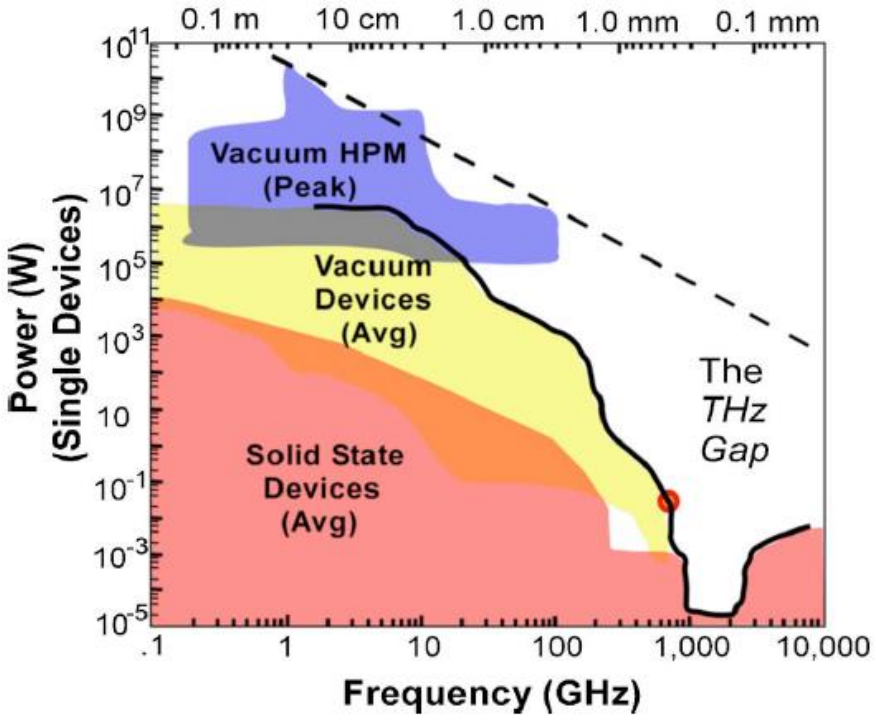

Fig. 1.2 Power vs frequency of compact and mobile, average power (single) devices. (Reproduced from Ref: [40])

Table 1.1 History of oversized BWOs at Niigata University

Year	Output power (kW)	Frequency	Content of work	D_s/λ*
2007[22]	500	K-band	Experimental work	2.7
2007[31]	200	Q-band	Experimental work	4.0
2014[28, 30]	10	G-band	Experimental work	18.0

* D_s = average diameter of the SWS

λ = free space wavelength of the output electromagnetic wave

Table 1.2 Brief history of TWTs

Year	Output power	Frequency	Content of work	Remark
2008[33]	50 mW	0.65 THz	Experimental work	Folded waveguide TWT
2011[34]	100 W	140 GHz	Numerical work	Folded waveguide TWT
2012[35]	152 kW	Q-band	Experimental work	Gyrotron TWT
2013[36]	56 W	0.22 THz	Numerical work	Ridge-vane-loaded folded waveguide TWT
2014[37]	112 kW	W-band	Experimental work	Gyrotron TWT
2015[38]	500 mW	G-band	Experimental work	Novel TWT harmonic terahertz amplifier
2016[39]	500 W	X/Ku-band	Numerical and experimental work	TWT

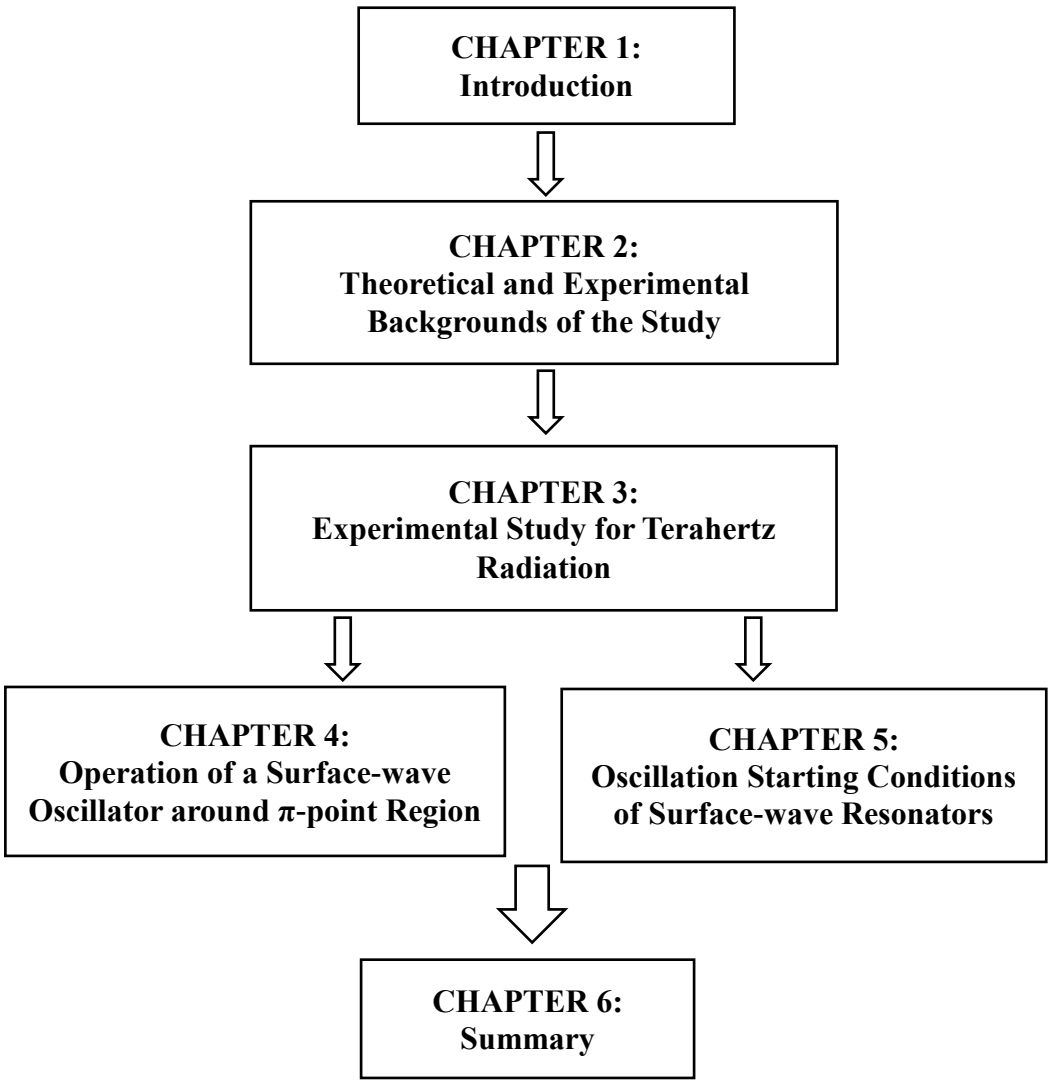

Fig. 1.3 Flowchart of the dissertation.

References

[1] R. Köhler, A. Tredicucci, F. Beltram, H. E. Beere, E. H. Linfield, A. G. Davies, D. A. Ritchie, R. C. Iotti, F. Rossi, "Terahertz semiconductor-heterostructure laser," Nature. 417, pp. 156-159. 2002.

[2] S. P. Mickan, and X. C. Zhang, "T-ray sensing and imaging," Int. J. High Speed Electron. Syst. 13, 601, 2003.

[3] V. M. Zolotarev, R. K. Mamedov, A. N. Bekhterev, and B. Z. Volchek, "Spectral emissivity of a globar lamp in the 2–50-μm region," J. Opt. Technol., vol. 74, 378–84, 2007.

[4] K. Charrada, G. Zissis, and M. Aubes, "Two-temperature, two-dimensional fluid modelling of mercury plasma in high-pressure lamps," J. Phys. D: Appl. Phys., vol. 29, 9, pp. 2432–8, 1996.

[5] J. Horvat, and R. A. Lewis, "Peeling adhesive tape emits electromagnetic radiation at terahertz frequencies," Opt.Lett. vol. 34, 2195–7, 2009.

[6] D. Haneman, and N. McAlpine, "Cleavage luminescence from silicon," Phys. Rev. Lett., vol. 66, 758–61, 1991.

[7] L. A. Yang, S. Long, X. Guo, and Y. Hao, "A comparative investigation on sub-micrometer InN and GaN Gunn diodes working at terahertz frequency," J. Appl. Phys., vol. 111, 104514, 2012.

[8] S. P´erez, T. Gonz´alez, D. Pardo, and J. Mateos, "Terahertz Gunn-like oscillations in InGaAs/InAlAs planar diodes," J. Appl. Phys., vol. 103, 094516, 2008.

[9] R. K¨ohler, A. Tredicucci, F. Beltram, H. E. Beere, E. H. Linfield, A. G. Davies, D. A. Ritchie, R. C. Iotti, and F. Rossi, "Terahertz semiconductor-heterostructure laser," Nature, vol. 417, 156–9, 2002.

[10] J. H. Booske, R. J. Dobbs, C. D. Joye, C. L. Kory, G. R. Neil, G. S. Park, J. Park, and R. J. Temkin, "Vacuum electronic high power terahertz sources," IEEE Trans. Terahertz Sci.Technol., vol. 1, 54–75, 2011.

[11] R. A. Kehs, A. Bromborsky, B. G. Ruth, S. E. Graybill, W. W. Destler, Y. C. Carmwl, and M. C. Wang, " A high-power backward-wave oscillator driven by a relativistic electron beam," IEEE Trans. Plasma Sci., vol. PS-13, 6, Dec. 1985.

[12] X. Li, J. Wang, J. Sun, Z. Song, H. Ye, Y. Zhang, L. Zhang, and L. Zhang, "Experimental study on a high-power subterahertz source generated by an overmoded surface wave oscillator with fast startup," IEEE Trans. Electron Devices, vol. 60, no. 9, pp. 2931-2935, July 2013.

[13] H. A. Leupold, L. Kosa, G. McLane, A. S. Tilak, and E. Potenziani II, "Permanent magnet sources for extended interaction klystrons," J. Appl. Phys., vol. 70, 6624–6, 1991.

[14] J. R. Pierce, *Traveling wave tubes*, Van Nostrand, New York, 1950.

[15] V. L. Bratman, Y. K. Kalynov, and V. N. Manuilov, "Large-orbit gyrotron operation in the terahertz frequency range," Phys. Rev. Lett., vol. 102, 245101, 2009.

[16] M. A. Dem'yanenko, D. G. Esaev, B. A. Knyazev, G. N. Kulipanov, and N. A. Vinokurov, "Imaging with a 90 frames/s microbolometer focal plane array and high-power terahertz free electron laser," Appl. Phys. Lett., vol. 92**,** 131116, 2008.

[17] J. M. Byrd, W. P. Leemans, A. Loftsdottir, B. Marcelis, M. C. Martin, W. R. McKinney, F. Sannibale, T. Scarvie, and C. Steier, "Observation of broadband self-amplified spontaneous coherent terahertz synchrotron radiation in a storage ring," Phys. Rev. Lett., vol. 89, 224801, 2002.

[18] F. S. Rusin, and G. D. Bogomolov, “Orotron-An electronic oscillator with an open resonator and reflecting grating,” Proc. IEEE (Lett.), vol. 57, pp. 720-722, Apr. 1969.

[19] K. Mizuno, S. Ono, and Y. Shibata, “Two different mode interactions in an electron tube with a Fabry-Perot resonator-The Ledatron,” IEEE Trans. Electron Devices, vol. ED-20, pp. 749-752, Aug. 1973.

[20] A.V. Gunin, A. I. Klimov, S. D. Korovin, I. K. Kurkan, I. V. Pegel, S. D. Polevin, A. M. Roitman, V. V. Rostov, A. S. Stepchenko, and E. M. Totmeninov, “Relativistic X-band BWO with 3-GW output power,” IEEE Trans. Plasma Sci., vol. 26, no. 3, pp. 326-331, Jun. 1998.

[21] A. N. Vlasov, A. G. Shkvarunets, J. C. Rodgers, Y. Carmel, T. M. Antonsen, T. M. Abuelfadl, D. Lingze, V. A. Cherepenin, G. S. Nusinovich, M. Botton, and V. L. Granatstein, “Overmoded GW-class surface-wave microwave oscillator,” IEEE Trans. Plasma Sci., vol. 28, no. 3, pp. 550-560, Jun. 2000.

[22] S. Aoyama, Y. Miyazawa, K. Ogura, A. Sugawara, and M. Hirata, “Improved performance of oversized backward wave oscillator driven by weakly relativistic electron beam,” Fusion Sci. Tech., vol. 51, no. 2T, pp. 325-327, Feb. 2007.

[23] J. Benford, J. A. Swegle, and E. Schamiloglu, *High Power Microwaves*. 2nd ed. New York, USA: Taylor & Francis, 2007.

[24] J. H. Booske, “Plasma physics and related challenges of millimeter-wave-to-terahertz and high power microwave generation,” Phys. Plasma, vol. 15, 055502, Feb. 2008.

[25] G. D. Bogomolov, and F. S. Rusin, “Submillimeter orotorn with quasi-optical power output,” Radiotekh. Elektron, vol. 15, pp. 854-856, 1970.

[26] V. L. Bratman, V. A. Gintsburg, and Yu. A. Grishin, B. S. Dumesh, F. S. Rusin, and A. E. Fedotov, “Pulsed wideband orotrons of millimeter and submillimeter waves,” Radiophys. Quantum Electron, vol. 49, pp. 866-871, 2006.

[27] V. L. Bratman, B. S. Dumesh, A. E. Fedotov, P. B. Makhalov, B. Z. Movshevich, and F. S. Rusin, “Terahertz Orotrons and Oromultipliers,” IEEE Trans. Plasma Sci., vol. 38, no. 6, pp. 1466-1471, Jun. 2010.

[28] S. Magori, K. Ogura, T. Iwasaki, J. Kojima, K. Yambe, S. Kubo, T. Shimozuma, S. Kobayashi, and K. Okada, “Experimental study on G-band oversized backward wave oscillator driven by weakly relativistic electron beam,” Plasma Fusion Res., vol. 9, 3406032, Apr. 2014.

[29] W. He, L. Zhang, D. Bowes, H. Yin, K. Ronald, A. D. R. Phelps, and A. W. Cross, “Generation of broadband terahertz radiation using a backward wave oscillator and pseudospark-sourced electron beam,” Appl. Phys. Lett., vol. 107, 133501, Sep. 2015.

[30] S. Gong, K. Ogura, S. Nomizu, A. Shirai, K. Yamazaki, K. Yambe, S. Kubo, T. Shimozuma, S. Kobayashi, and K. Okada, “Oscillation starting conditions for oversized G-band (140 – 220 GHz) backward wave oscillator driven by weakly relativistic electron beam,” IEEE Trans. Plasma Sci., vol. 43, no. 10, pp. 3530-3536, Oct. 2015.

[31] K. Ogura, Y. Miyazawa, S. Aoyama, Y. Takamura, S. Tamura, and A. Sugawara, “Studies of a weakly relativistic oversized backward wave oscillator with disk cathode and rectangular corrugation,” IEEJ Trans. FM, vol. 127, no. 11, pp. 681–686, Nov. 2007.

[32] S. Bhattacharjee, J. H. Booske, C. L. Kory, D. W. van der Weide, S. Limbach, S. Gallagher, J. D. Welter, M. R. Lopez, R. M. Gilgenbach, R. L. Ives, M. E. Read, R. Divan, and D. C. Mancini, “Folded waveguide traveling-wave tube

sources for terahertz radiation," IEEE Trans. Plasma Sci., vol. 32, no. 3, pp. 1002–1014, Jun. 2004.

[33] K. E. Kreischer, J. C. Tucek, D. A. Gallagher, and R. E. Mihailovich, "Operation of a compact, 0.65 THz source," Proc. 33rd Int. Conf. on Infrared, Millimeter and Terahertz Waves, Pasadena, CA, 15-19 Sep. 2008.

[34] Y. Gong, H. Yin, L. Yue, Z. Lu, Y. Wei, J. Feng, Z. Duan, and X. Xu, "A 140-GHz two-beam overmoded folded-waveguide traveling-wave tube," IEEE Trans. Electron Devices, vol. 39, 3, pp. 847-851, Mar. 2011.

[35] R. Yan, Y. Luo, G. Liu, and Y. Pu, "Design and experiment of a Q-band Gyro-TWT Lloaded with Lossy dielectric," IEEE Trans. Electron Devices, vol. 59, 12, pp. 3612-3617, Dec. 2012.

[36] Y. Hou, Y. Gong, J. Xu, S. Wang, Y. Wei, L. Yue, and J. Feng, "A Nnovel ridge-vane-loaded folded-waveguide slow-wave structure for 0.22-THz traveling-wave tube," IEEE Trans. Electron Devices, vol. 60, 3, pp. 1228-1235, Mar. 2013.

[37] R. Yan, Y. Tang, and Y. Luo, "Design and experimental study of a high-gain W-Band Gyro-TWT with nonuniform periodic dielectric loaded waveguide," IEEE Trans. Electron Devices, vol. 61, no. 7, pp. 2564–2569, July 2014.

[38] J. Cai, X. Wu, and J. Feng, "Travelling-wave tube harmonic amplifier in terahertz and experimental demonstration," IEEE Trans. Electron Devices, vol. 62, 2, pp. 648-651, Feb. 2015.

[39] A. B. Danilov, D. N. Zolotykh, I. P. Medvedkov, A. I. Petrosyan, A. D. Rafalovich, V. I. Rogovin, S. O. Semenov, V. A. Senchurov, and L. A. Shtern, "Development of X/Ku-broadband powerful TWT," 2016 International Conference on Actual Problems of Electron Devices Engineering (APEDE), Saratov, Russia, Sep. 2016.

[40] J. H. Booske, “Plasma physics and related challenges of millimeter-wave-to-terahertz and high power microwave generation,” Physics of Plasmas 15, 055502 (2008).

Chapter 2

Theoretical and Experimental Backgrounds of the Study

2.1. Introduction

Electron beam and slow-wave structure (SWS) have been employed in producing of high-power microwave radiation [1], [2]. In vacuum electronic devices, parameters of electron beam and SWS determine the characteristics of the radiation. Dispersion relation of the SWS can be recognized by numerical method based on the parameters of the SWS. With electron beam line and dispersion relation, radiation frequency, operation region: BWO or TWT, Cherenkov or Cyclotron interaction, absolute or convective instability can be predicted. In the experiment, the electron beam is generated by disk-type cold cathode. Parameters of the cathode determine characteristics of the electron beam. Parameters of cathode and SWS employed in the study are changed for different rating of radiation while other experimental set-up is unchanged.

In Section 2.2, theoretical background of the study is briefly explained. The SWS used in the BWO is presented in Section 2.3, and the numerical analysis for the dispersion relation of the SWS is described in Section 2.4. Experimental devices are presented in Section 2.5. Experimental set-up and operation are presented in Section 2.6.

2.2. Theoretical Background of the Study

Vacuum electronic devices utilize electron beam as an energy source. When the electron beam propagates along the direction of external magnetic field, four beam modes; slow and fast space charge modes, and slow and fast cyclotron modes, exit. The space charge and cyclotron modes are $\omega = k_z v_0$ and $\omega = k_z v_0 \pm \Omega/\gamma_0$, respectively. Here, γ_0 is a relativistic factor, k_z is wave number, Ω is the angular electron cyclotron frequency and its sign + and – mean, respectively, fast and slow modes. All beam modes are shown in Fig. 2.1.

When the electron beam flows through the waveguide, electromagnetic wave is developed in it due to the acceleration of the electron. In a straight waveguide, the phase velocity of the electromagnetic mode v_p is larger than the velocity of light c and beam velocity v_b. By means of SWS, v_p is slow down and reduced to v_b. And the energy exchange between the beam mode and the electromagnetic (EM) mode occurs when $v_p < v_b$. Cherenkov radiation occurs when the space charge mode interacts with the EM mode, and Cyclotron interaction is by the cyclotron and EM modes. The SWS can support slow waves both in the forward (positive group velocity) and backward (negative group velocity) regimes. If the electron beam interacts with the EM mode with the positive phase and group velocity, the device operates in the manner of TWT. At the upper cutoff frequency where normalized wave number of the SWS period is equal to π-radian, the phase velocity is positive and group velocity is zero. When the group velocity of the interacting EM mode is negative while the phase velocity is positive, the device operates in the manner of BWO [3].

2.3 Slow-wave Structure

Periodically corrugated SWSs have been extensively used in microwave devices [4]. In the study, rectangular-corrugated waveguides are used as the SWSs.

The SWSs used in the study are in cylindrical geometry and oversized; model of the SWS with rectangular corrugations is shown in Fig. 2.2. Here, oversized means the diameter of the SWS D_s is two or more times larger than the free space wavelength of the output electromagnetic wave λ. Oversized SWS is used to increase the operation frequency and the power handling capability. For terahertz wave regions, D_s/λ is much larger than 1 and the cylindrical SWS is virtually an open cavity. The slow waves in the oversized SWS are also surface waves concentrated in the vicinity of the walls like Oroton and Smith-Purcell free electron laser [5]-[8].

Surface wave is of electromagnetic wave developed along the surface of a medium. Electromagnetic surface wave on corrugated metal surface has been numerically studied in [9]. Due to the periodic of the corrugated metal surface, dispersion relation of the surface wave has backward wave regions. In addition, the surface wave is of slow wave and evanescent wave to the direction away from the corrugated metal surface. Field lines and Poynting vectors in corrugated waveguides were numerically analyzed in [10], which pointed out that electric field E_z and radial distribution of Poynting vector P_z are maximum on the axis $r = 0$ and $r < R_0 - h$ in the case of volume wave, and E_z and P_z are largest at a peripheral region near R_0 and $r > R_0 - h$ in the case of surface wave. For non-oversized SWSs, a strong field of volumetric waves developed near the axis [11], [12], but for oversized SWSs, the fields of surface waves concentrate near the SWS wall [13].

As the discharge in the SWS by the strong electric field is serious at higher power, the sinusoidal corrugations are preferable for the extremely high power or more of the GW oscillator. Output powers in the range of hundreds of kW were obtained by the K- and Q-band BWOs using sinusoidal corrugated SWSs [14], [15]. But for higher frequency radiations, the sinusoidal corrugations are very difficult to be fabricated. To overcome the constructional difficulty of sinusoidal corrugation, Ref. [16] studied the rectangular shape corrugations for the radiation

of a few hundreds of kW for the K-band BWO. As the discharge in the SWS may not be serious problem for the moderate power level of the MW or less, and in addition the rectangular corrugations can be fabricated more easily and accurately than the sinusoidal corrugations, the rectangular corrugations have being used for higher frequency with moderate power radiation.

2.4. Numerical Analysis of SWS

A cylindrical waveguide with rectangular corrugations on the wall is used as SWSs in the study. The average radius, corrugation amplitude, corrugation width, and periodic length of the SWS are denoted, R_0, h, d, and z_0, respectively. The model of the SWS and electron beam is shown in Fig. 2.2. The corrugation wave number is defined as $k_0 = 2\pi/z_0$. A guiding magnetic field B_0 is applied in the z-direction and an infinitesimally thing annular electron beam of radius R_b propagates along B_0. We consider a linear model assuming a temporal and spatial phase factor of perturbed quantities of $\exp[i(k_z z + m\varphi - \omega t)]$. Here, m is the azimuthal mode number, k_z is the axial wave number, and ω is the angular frequency. The dispersion curve of the SWS is obtained by a numerical method based on the mathematical formula in [17]-[19]. In the following, we briefly summarize the mathematical formulation.

The components of the axial electromagnetic field inside the beam (region I, $r < R_b$) may be expressed as

$$E_{1z}^{I} = \sum_{p=-\infty}^{\infty} A_{Ep} J_m(x_p r),$$

$$B_{1z}^{I} = \sum_{p=-\infty}^{\infty} \frac{i}{c} A_{Bp} J_m(x_p r). \qquad (2.1)$$

And the outside of the beam in the waveguide (region II, $R_1 > r > R_b$),

$$E_{1z}^{II} = \sum_{p=-\infty}^{\infty} \left[D_p J_m(x_p r) + E_p N_m(x_p r) \right],$$

$$B_{1z}^{II} = \sum_{p=-\infty}^{\infty} \frac{i}{c}\left[F_p J_m\left(x_p r\right) + G_p N_m\left(x_p r\right)\right]. \tag{2.2}$$

Here, J_m and N_m are respectively the mth order Bessel function of the first kind and the second kind, $k_p = k_z + pk_0$, p is Floquet's harmonic number and

$$x_p^2 = \frac{\omega^2}{c^2} - k_p^2 \cdot \tag{2.3}$$

The constants A_{Ep}, A_{Bp}, D_p, E_p, F_p, and G_p are the electromagnetic field coefficients of the vacuum regions.

Using the four independent equations obtained at the beam surface, the electromagnetic fields in region II are correlated with those in region I. Hence, the coefficients D_p, E_p, F_p, and G_p are expressed in terms of A_{Ep} and A_{Bp}. The other field components can be derived from the axial electromagnetic fields.

The normal functions for cylindrical systems are the Bessel functions, i.e., J_m and N_m. They can be used for non-oversized SWSs in which strong electromagnetic fields are near the axis. However, the surface waves in oversized SWS are localized very close to the SWS wall. In this case, electromagnetic modes have imaginary radial wave numbers and the modified Bessel functions, i.e., I_m and K_m are used instead of J_m and N_m.

In the rectangular corrugation region (region III, $R_2 > r > R_1$), the electromagnetic field are expressed as a sum of standing waves that satisfy the boundary conditions on the corrugation walls. The normal modes of the system can be derived subject to the given boundary conditions. Together with the conditions at the beam, electromagnetic fields in all regions of the SWS in terms of A_{Ep} and A_{Bp} of (2.1), and the boundary conditions for the system in Fig. 2.2 can be expressed, respectively, in the z-direction and azimuthal direction as,

$$D^{(Z+)} \cdot A_E + D^{(Z-)} \cdot A_B = 0,$$

$$D^{(T+)} \cdot A_E + D^{(T-)} \cdot A_B = 0 . \quad (2.4)$$

Here, A_E and A_B are column vectors with elements A_{Ep} and A_{Bp}, and $D^{(Z\pm)}$ and $D^{(T\pm)}$ are matrixes of an infinite rank. The superscript (Z) and (T) means the z-direction and azimuthal direction on the SWS boundary. The superscript (+) and (-) mean the electric fields originated from E_{1z}^{I} and B_{1z}^{I}, respectively. And then, they are summarized in a matrix form as,

$$\begin{bmatrix} D^{(Z+)} D^{(Z-)} \\ D^{(T+)} D^{(T-)} \end{bmatrix} \cdot \begin{bmatrix} A_E \\ A_B \end{bmatrix} = 0 . \quad (2.5)$$

The dispersion relation is obtained from the condition that (2.5) has a nontrivial solution. After restricting the space harmonics to a finite number, the dispersion relation is given by,

$$\det \begin{bmatrix} D^{(Z+)}(\omega, k_z) D^{(Z-)}(\omega, k_z) \\ D^{(T+)}(\omega, k_z) D^{(T-)}(\omega, k_z) \end{bmatrix} = 0 . \quad (2.6)$$

For $m = 0$, $D^{(Z-)}$ and $D^{(T+)}$ become zero matrices. From the dispersion equation (2.6), $\det[D^{(Z+)}] = 0$ gives transverse magnetic (TM) modes and $\det[D^{(T-)}] = 0$ gives transverse electric (TE) modes. Pure TM and TE modes are the normal modes in this case.

2.5. Experimental Background of the Study

In the experimental set-up, pulse power system, electron beam generation, SWS, guiding magnetic coil, detecting system and control units are included.

2.5.1. Pulse power system

In the laboratory, we use two kinds of pulse power devices. For higher voltage pulse power generation of approximately 20–100 kV, the combination of Marx generator and PFL is used. Magnetic pulse compressor (MPC) is for lower voltage pulse power generation of less than 30 kV.

2.5.1.1 Marx generator and PFL

Marx generator as well as PFL is of a pulse power source. In the laboratory, they are cascaded to generate the desired pulse voltage.

In the laboratory, Marx generator of IG-H200 made by Nichicon Corporation is used. The photograph of the Marx generator and its specifications are shown in Fig. 2.3 and Table 2.1, respectively.

PFL of a coaxial cable type is used in the laboratory. It applies high density pulse power to a cathode by compressing the impulse voltage generated from the Marx generator. As the inner and outer conducting and insulating materials, stainless steel and pure water are used in the PFL. The inner diameter of the outer conductor and outer diameter of the inner conductor are 261.4 and 89.2 mm, respectively. The length of PFL is in 1 m. Pure water with high dielectric strength and high dielectric constant is possible to constitute a compact line in the high voltage region with a low characteristics impedance. In order to maintain the electrical characteristics of the pure water as much as possible, it is necessary to make the water circulated by a pump though the ion exchange resin filter. Photograph of PFL is shown in Fig. 2.4(a). The electrical characteristics of the PFL are shown in Table 2.2. Duration of the pulse formed by the PFL is $2l\sqrt{\varepsilon_s}/c$ = 60 nsec. Where l is the length of the PFL, ε_s is the dielectric constant of pure water, 81, and c is the velocity of the light. Typical beam voltage and current wave forms by the PFL are shown in Fig. 2.4(b).

2.5.1.2. MPC

MPC is a highly non-linear process and uses inductors as switches. It is possible to achieve higher voltage pulse steepness and higher maximal values of reactor currents. It utilizes the magnetized inductors in conjunction with capacitors to shape input pulses into narrow output pulses of much higher current. In the laboratory, MPC (3010S-25LN, manufactured by Suematsu Electronics Mfg. Co.,

Ltd.) consists of two units: pulse power unit (PPU) and charging control unit (CCU). The specifications and the photograph of the MPC are shown in Table 2.3 and Fig. 2.5(a), respectively. In the figure, the upper and lower units are of CCU and PPU. Typical beam voltage and current wave forms by the MPC are shown in Fig. 2.5(b).

2.5.2. Electron beam generation

Two electrodes are used as an anode and cathode to form an electron beam diode. When a very high voltage is applied to the diode, plasma will appear at the surface of the cathode, and a charge particle source is formed on the vicinity of the cathode. By the high intensity electric field, electrons from the cathode are accelerated toward the anode. As a result, a flow of electron or an electron beam is formed between the cathode and anode.

2.5.2.1. Electron beam diode

We use a hollow anode and disk-type cold cathode to get an annular electron beam. Foilless stainless steel is used as the anode, and oxygen-free copper or steel is used as the cathode. We use two types of cathode surface: bare cathode surface and velvet attached at the outer ring of the cathode surface for the field-enhanced explosive emission and surface-flashover explosive emission, respectively. Velvet or surface roughness on the emission surface is required for uniform electron emission. They both are useful in rather high voltage of above 60 kV. For low voltage of less than 60 kV, the cathode with velvet is suitable. Uniform electron beam generation utilizing a disk-type cold cathode in the weakly relativistic energy region is presented in [20], [21]. Photographs of the anode and cathodes are shown in Fig. 2.6. In the experiment, a beam limiter that has different diameter is used as the anode to vary the electron beam diameter. The distance between the anode and cathode (A-K gap) can be varied from 0 to 25 mm by using a linear introducer. In the experiment, the A-K gap is set normally at 10 mm. The configuration of the A-K gap of the diode is shown in Fig. 2.7.

2.5.2.2. Electron beam

The flow of electron beam emitted from the cathode surface is confined in the axial direction by the magnetic field coils. The generated beam pattern is examined as a burn pattern in a thermal-sensitive paper placed on a beam collector located at 228 mm away from the anode. The electron beam is in an annular shape and the thickness is typically 2–3 mm. The diameter of the beam depends on the diameter of the cathode and beam limiter. The burn patterns of the electron beam shapes emitted from the cathode with and without velvet are shown in Fig. 2.8.

2.5.3. SWSs

In the laboratory, the cylindrical SWSs with the rectangular corrugations made of aluminum are used. The parameters of the SWS determine the characteristics of the radiation patterns. Photographs and parameters of SWSs for upper cutoff frequency of 0.1, 0.35 and 0.5 THz radiation used in the experiment are shown in Fig. 2.9 and Table 2.4, respectively. Each module of SWS for 0.1 THz has 10, 20, 40, and $80z_0$. For 0.35 THz radiation, each module has 40, 60 and $80z_0$, and for 0.5 THz radiation, each module has 80, 120, and $160z_0$. Two or more modules are combined to get other lengths presented in the study.

2.5.4. Guiding magnetic field

Guiding magnetic field is used to confine the propagation of electron beam in the axial direction. In the laboratory, ten magnetic field coils made by Techo Electric Industy Co., Ltd. is used. The magnetic field intensity can be varied from 0 to 1 T by varying the input dc current. Rated power is approximately 150 kVA where rated voltage and maximum current are of 300 V and 500 A, respectively. We normally set up the magnetic field at approximately 0.82 T in the experiment. The photograph of ten magnetic field coils and arrangement of the guiding magnetic field in the experiment are shown in Fig. 2.10 and 2.11. Table 2.5 shows the axial magnetic field set up value by the different dc current.

2.5.5. Detecting system

Beam voltages and beam currents are detected by voltage divider and Rogowski coil, respectively, and radiated signals are picked up by horn antennas, waveguides and high pass filters. They are arranged that the beam voltages, beam currents and radiated signals can be observed simultaneously.

2.5.5.1. Voltage divider

By a voltage divider, beam voltages are measured. The divider circuit is shown in Fig. 2.12. Ceramic resistor R_1 is used as high voltage application in the circuit. At both ends of BNC cable, $R_2 + R_3 = R_4 + R_5 = 50\ \Omega$ which is matched with the PFL to suppress reflection. The beam voltages are reduced to 1/13572 by the divider circuit and measured by oscilloscope.

2.5.5.2. Rogowski coil

The electron beam current is monitored by a Rogowski coil designed for monitoring nanosecond order current pulse. The coil is located at the entrance of the SWS and encircled the electron beam completely. The configuration diagram of the Rogoswki coil and integrated circuit is shown in Fig. 2.13.

2.5.5.3. Horn antenna, waveguide and high pass filter

The radiated signals are picked up by horn antennas and rectangular waveguides. Depending on the radiated frequencies and powers, different bands of horn antennas and waveguides, and several ranges of attenuation are set up in the experiment. The output powers are detected by crystal detectors of ELVA-1 ZBD-08. They are typically located 600 mm away from the output window. Photographs of horn antennas and waveguides used in the experiment and their cutoff frequencies are shown in Fig. 2.14 and Table 2.6, respectively. The cutoff frequency values are of Electronic Industries Alliance (EIA) standard rectangular waveguides values [22]. To confirm the radiated frequency is over the specific value or not, high pass filters (HPFs) of 0.3, 0.35 and 0.4 THz are used for the

operation of SWRs (0.35 THz) and (0.5 THz) cases. Photographs of HPFs are shown in Fig. 2.15.

2.5.6. System control units

The guiding magnetic field coils control, Marx generator charging control, output voltage control for the PFL and MPC, and beam current control systems are set up in the laboratory.

2.5.6.1. Guiding magnetic field coils control

The photograph of the power supply controller for the guiding magnetic field coils is shown in Fig. 2.16. Left side control unit is for the magnetic field power supply control, and right side control unit is for dc current source.

2.5.6.2. Marx generator charging control

Charging voltage of the Marx generator is of very high voltage. So in accordance to be safe to the operator, remote control charging method is used in the laboratory. Sequence controller shown in Fig. 2.17 is used for the Marx generator charging control. The upper unit in the figure is for the control of discharge time interval, and the lower unit is for the charging voltage control.

2.5.6.3. Output voltage control for the PFL and MPC

The PFL is connected to the electron beam diode through a gap-switch to vary the PFL output voltage. The gap-switch has two identical dome-shaped brass electrodes, and is a gas-pressurized and self-breaking spark gap. The output voltage of the PFL is an increasing function of the gap distance of the switch, and it can be varied by adjusting the handle connected to one side of the gap-switch. The photograph of the gap-switch with the adjusting handle is shown in Fig. 2.18.

The output voltage of MPC can be varied by adjusting the control knob at PPU, shown in Fig. 2.5(a).

2.5.6.4. Beam current control

The electron beam current is a decreasing function of the A-K gap. The shorter the A-K gap is, the higher the electron beam current flows. The A-K gap distance control handle shown in Fig. 2.19 is attached to the cathode of the electron beam diode. Different electron beam current can be obtained by adjusting the handle. The handle is normally set-up at 4.5 mm which corresponds to the A-K gap of 10 mm.

2.6. Experimental Set-up

The schematic diagram of the experimental set-up and complete diagram of the experimental set-up are shown in Fig. 2.20 and 2.21, respectively. The electron beam diode and SWS are placed in a vacuum tube where the pressure of less than 10^{-5} torr. The output terminals of the PFL or MPC are connected to the anode and cathode of the diode. The PFL is supplied by the Marx generator, and a gap-switch is placed at the end of the PFL for the output voltage adjustment. The A-K gap is typically set up at 10 mm and can be varied by adjusting the current adjusting handle. A beam limiter is placed at the entrance of the electron beam to the SWS to prevent the erosion of the SWS surface. The guiding magnetic field coils cover the electron beam diode, SWS and flow of electron beam in the vacuum tube to confine the electron beam propagation in the axial direction. The radiation signal detecting system is placed typically 600 mm away from the output window by ± 5 or 10 degree of the reference frame. A Rogoswki coil is placed in front of the output window, and the resistive divider is between the gap-switch and electron beam diode. All detecting signals are displayed by the oscilloscope.

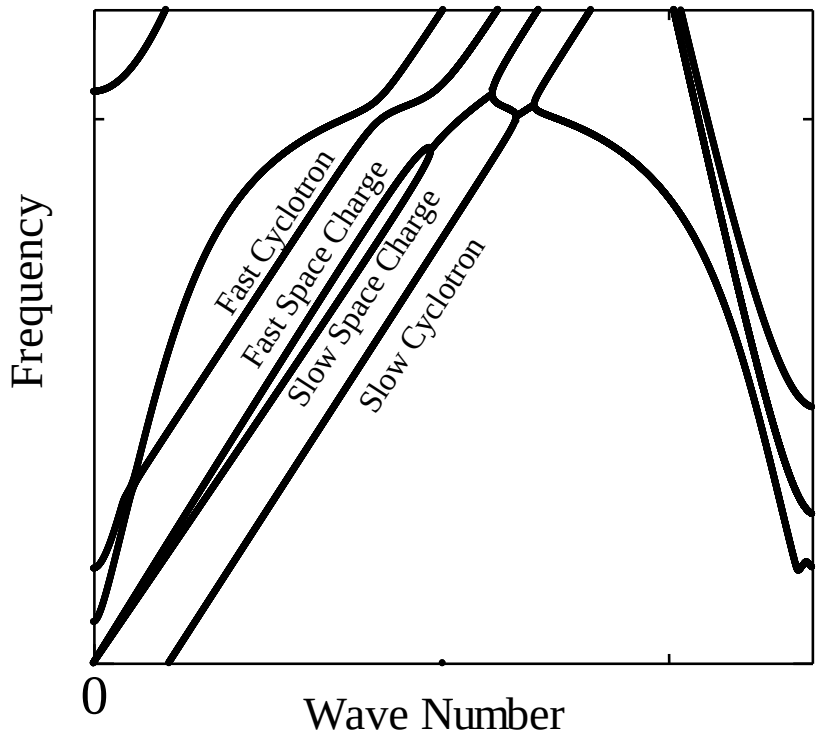

Fig. 2.1 Dispersion relation of beam modes.

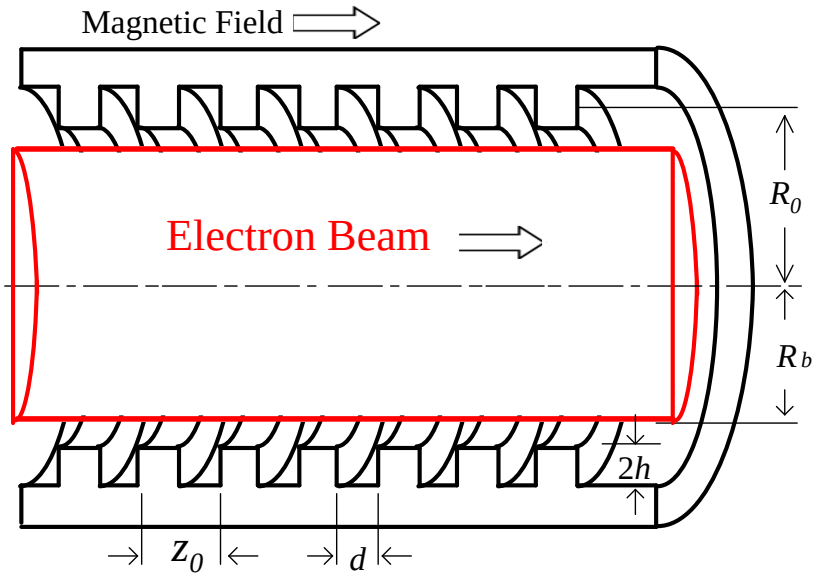

Fig. 2.2 Model of analysis: a rectangularly corrugated SWS and annular beam. A guiding magnetic field B_0 is applied uniformly in the axial direction. An electron beam is propagating along the magnetic field.

Fig. 2.3 Photograph of the Marx generator.

Fig. 2.4(a) Photograph of the PFL.

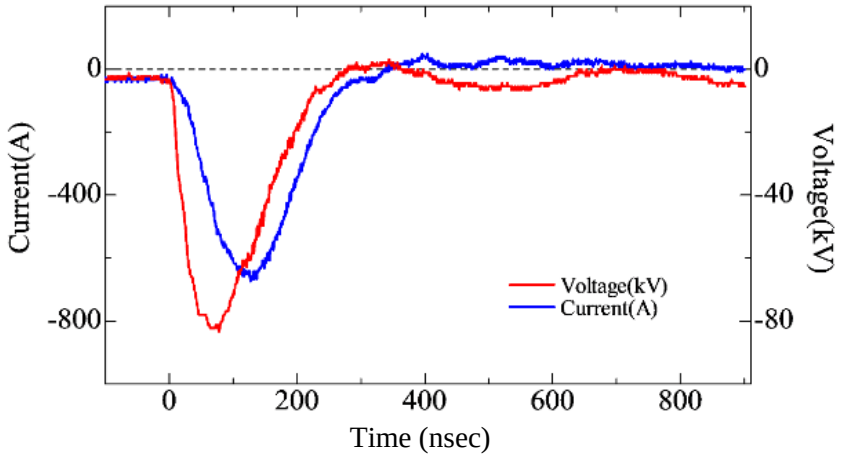

Fig. 2.4(b) Typical beam voltage and current wave forms by the PFL.

Table 2.1 Specifications of the Marx generator

Model	IG-H200
Nominal voltage	200 kV
Rated voltage	160 kV
Total capacity	0.05 μF
Utilization ratio	80%
Standard waveform	1.2/50 μsec
Maximum charging energy	1.0 kJ
Input voltage	100 V ± 10%, 50 Hz

Table 2.2 Electrical Characteristics of the PFL

Capacitance per unit length, C	4.14 (nF/m)
Inductance per unit length, L	215 (nH/m)
Characteristic impedance, Zc	7.21 (Ω)

Table 2.3 Specifications of the MPC

Model	MPC3010S-25LN
Nominal voltage	30 kV
Rated voltage	AC 100V/ 50–60 Hz
Cooling - Air	
Insulation - Air	

Fig. 2.5(a) Photograph of the MPC.

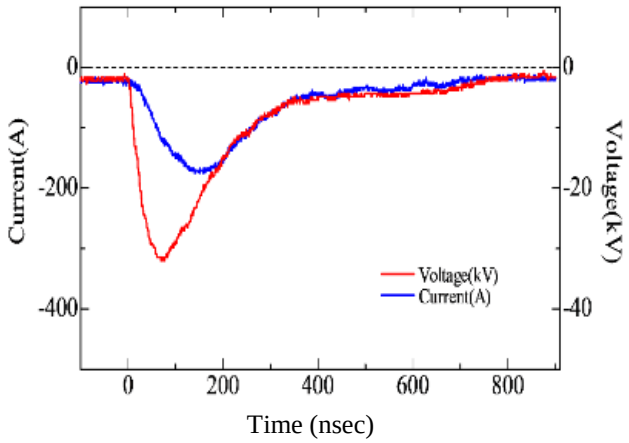

Fig. 2.5(b) Typical beam voltage and current wave forms by the MPC.

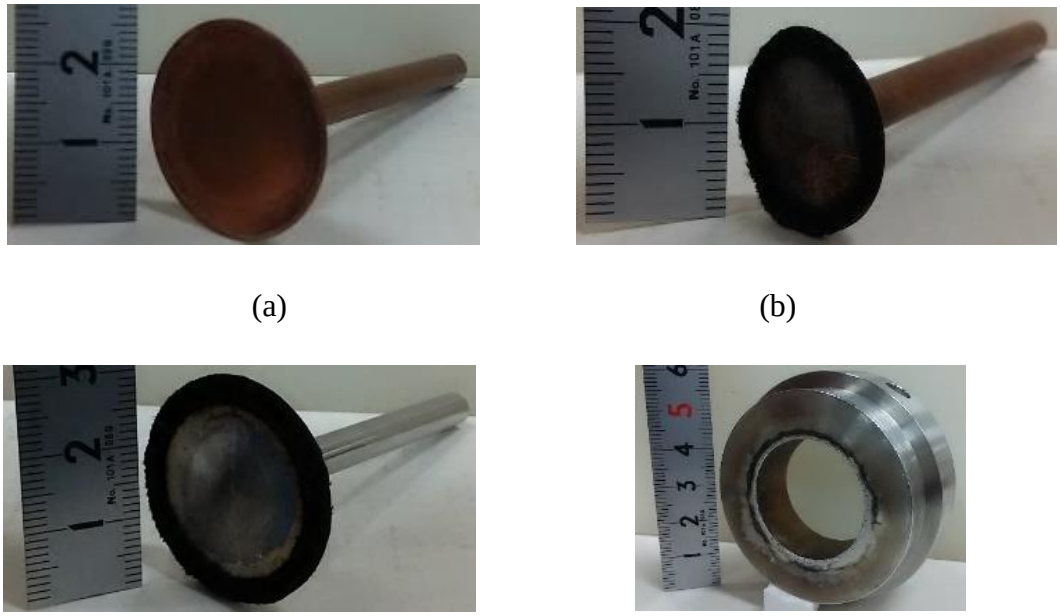

(a) (b)

(c) (d)

Fig. 2.6 Photographs of cathodes: (a) copper cathode with a bare surface (diameter 29 mm), (b) copper cathode with velvet on the surface (diameter 20 mm), c) steel cathode with velvet on the surface (29.5 mm), and (d) beam limiter made of steel used as an anode (inner diameter 29.7 mm).

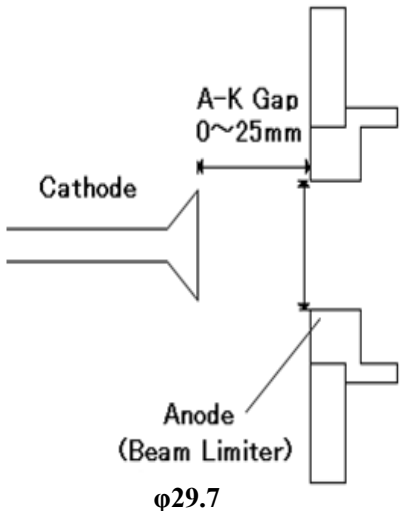

Fig. 2.7 Configuration of the A-K gap of the diode.

Table 2.4 Parameters of SWSs used in the experiment

Upper cutoff frequency	**$2R_0$ (mm)**	**$2h$ (mm)**	**d (mm)**	**z_0 (mm)**
0.1 THz	30.2	0.6	0.3	0.5
0.35 THz	29.85	0.15	0.15	0.25
0.5 THz	29.775	0.075	0.15	0.25

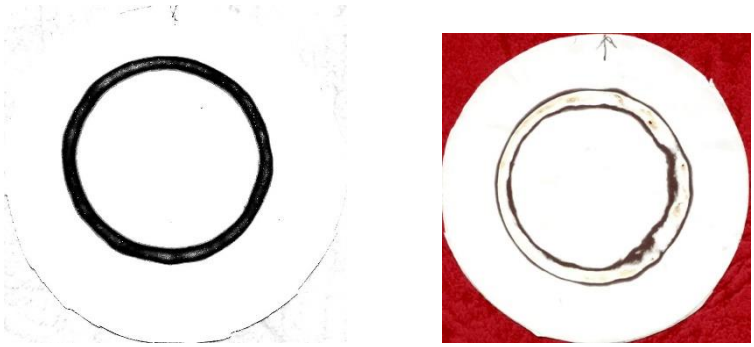

(a) (b)

Fig. 2.8 Burn patterns of electron beam for a disk cathode of diameter 29 mm. (a) With velvet with beam limiter diameter of 29.5 mm: outer and inner diameter of 29.5 and 26 mm. (b) Without velvet with beam limiter diameter of 29.7 mm: outer and inner diameter of 29.7 and 25.6 mm.

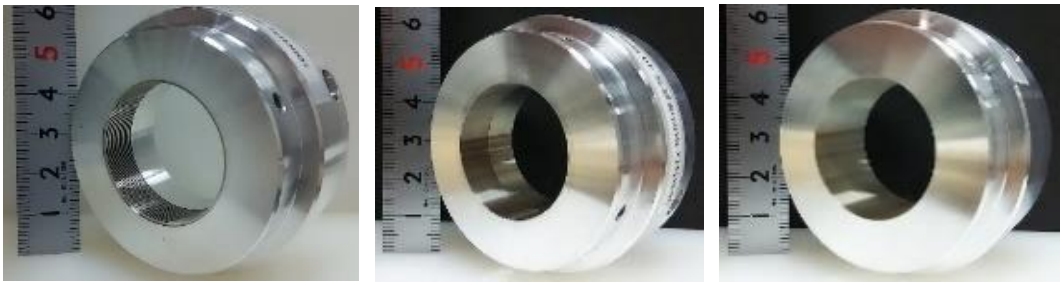

(a) (b) (c)

Fig. 2.9 Photographs of SWSs: (a) with $20z_0$ for the SWO (0.1 THz), (b) with $40z_0$ for the SWR (0.35 THz), and (c) with $80z_0$ for the SWR (0.5 THz).

Fig. 2.10 Photograph of magnetic field coils.

Table 2.5 Input dc current vs axial magnetic field

Control setting point	**Input dc current (A)**	**Axial magnetic field (T)**
1	36.6	0.0789
2	86.7	0.177
3	138.4	0.276
4	188.6	0.375
5	242.7	0.473
6	291.6	0.572
7	345.2	0.67
8	398.6	0.769
9	449.6	0.868
10	501.4	0.986

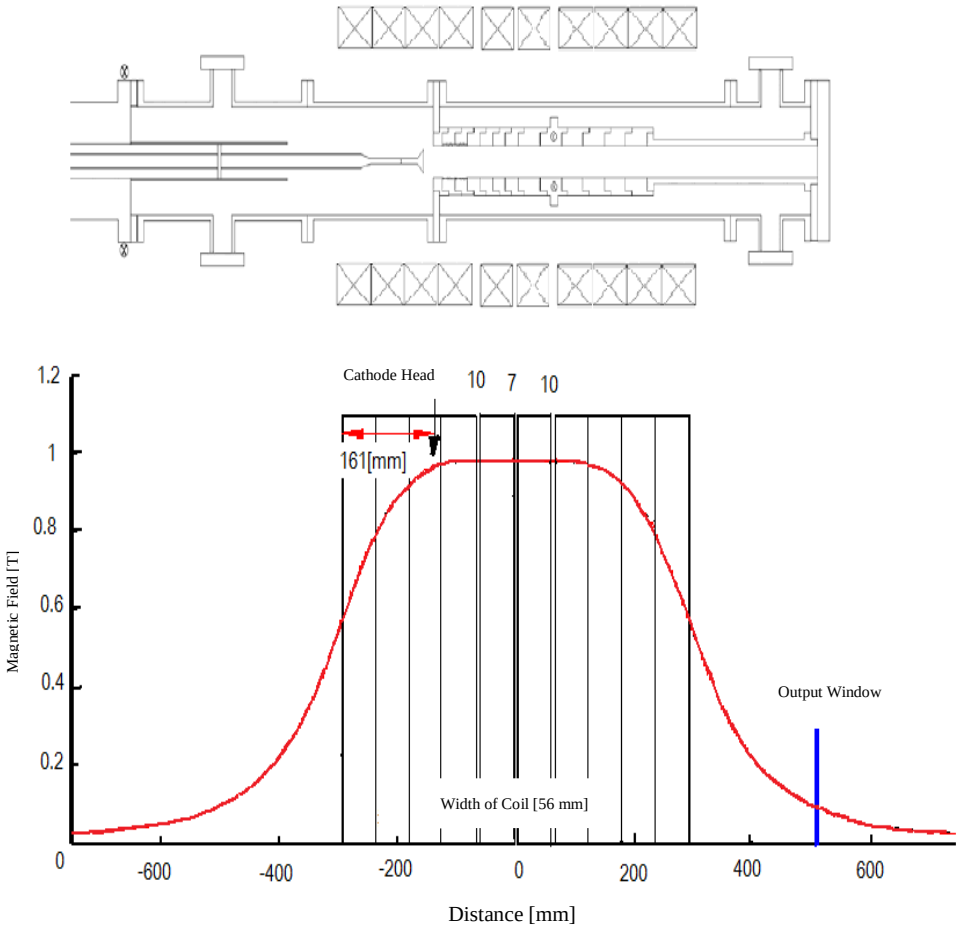

Fig. 2.11 Arrangement of the guiding magnetic field in the experiment.

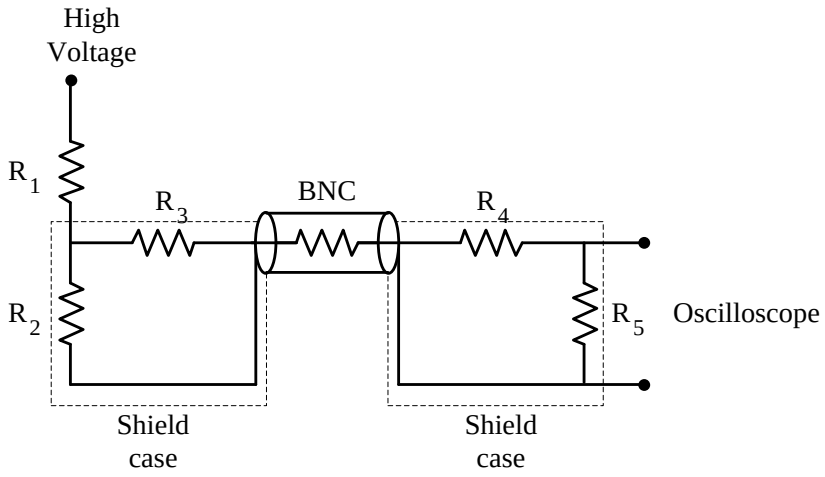

Fig. 2.12 Voltage divider for beam voltage measurement: R_1 = 4.5 kΩ, R_2 = 10 Ω, R_3 = 39 Ω, R_4 = 47 Ω, and R_5 = 3.3 Ω.

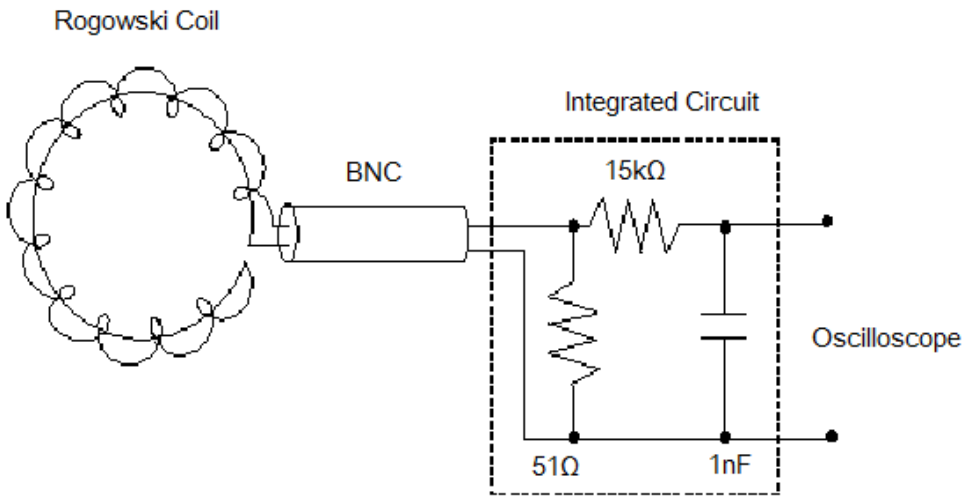

Fig. 2.13 Configuration diagram of the Rogoswki coil and integrated circuit.

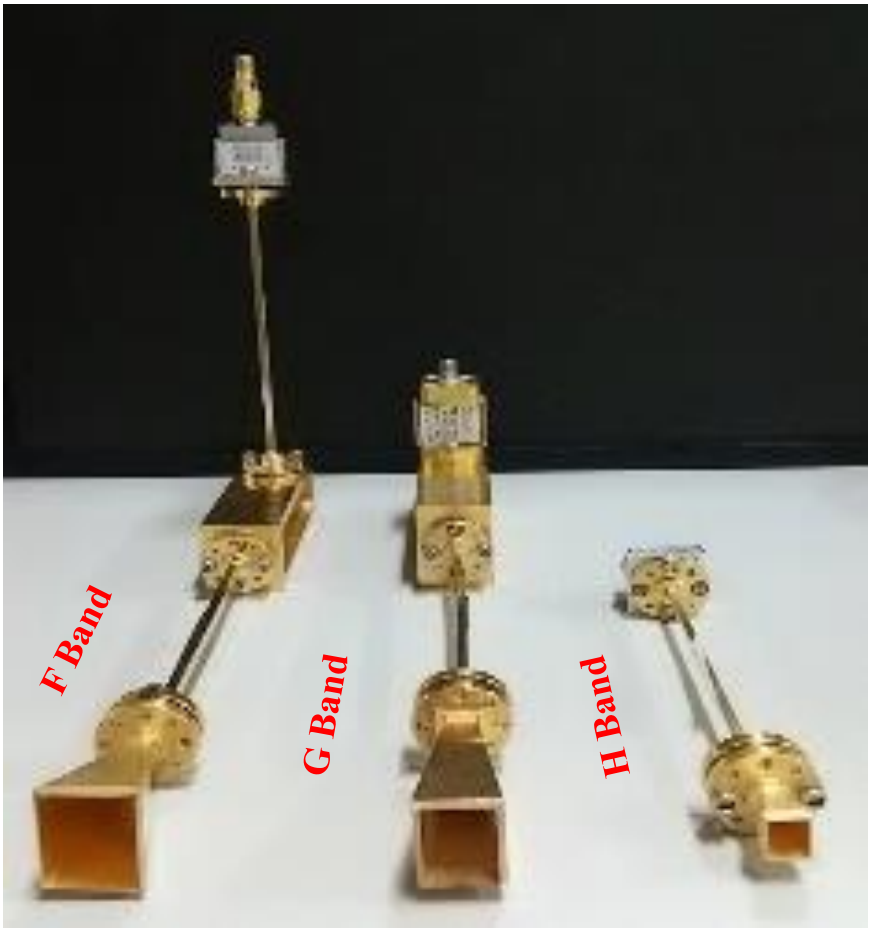

Fig. 2.14 Photographs of F-, G-, and H-band horn antennas used in the experiment.

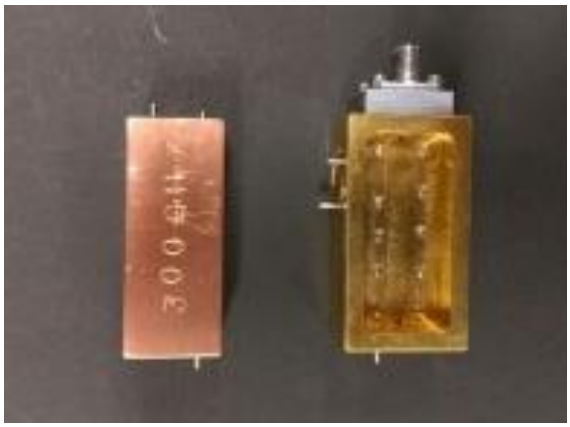

(a) (b)

(c) (d)

Fig. 2.15 Photographs of HPFs with cutoff frequency of (a) 0.27 THz, (b) 0.3 THz, (c) 0.35 THz, and (d) 0.4 THz.

Fig. 2.16 Photograph of the power supply controller for the guiding magnetic field coils.

Fig. 2.17 Sequence controller for the Marx generator charging control.

Table 2.6 Cutoff frequency of waveguides [22]

Band	**Recommended Frequency Range (GHz)**	**TE_{01} Cutoff Frequency (GHz)**	**EIA Designation WR-XX**
F	90.0–140.0	73.840	WR-8
G	140.0–220.0	115.750	WR-5

Fig. 2.18 Gap-switch with the adjusting handle.

Fig. 2.19 Electron beam current control handle.

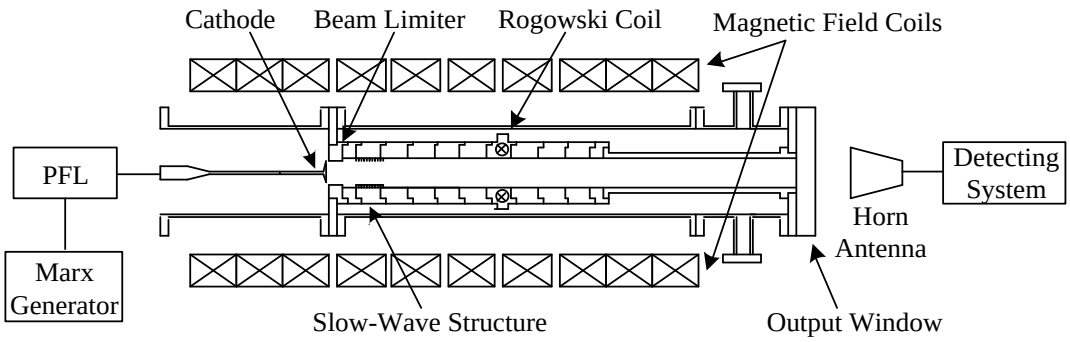

Fig. 2.20 Schematic diagram of the experimental set-up.

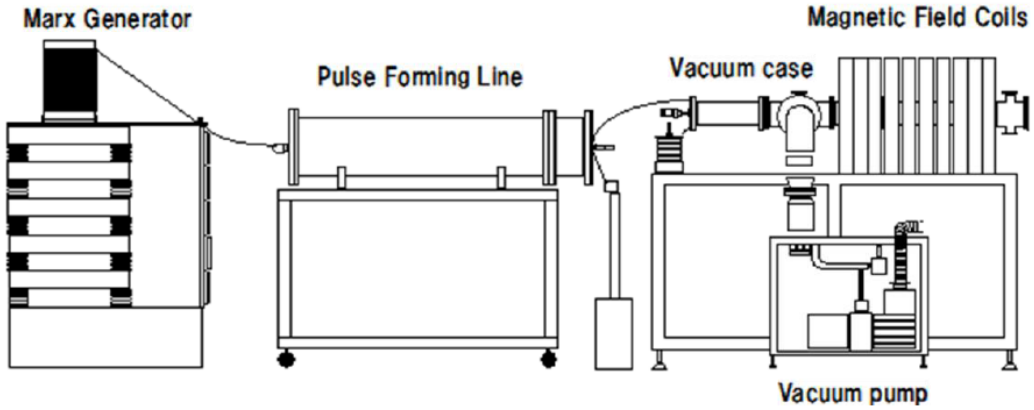

Fig. 2.21 Complete diagram of the experimental set-up.

References

[1] Y. Carmel, J. Ivers, R. E. Kribel, and J. Nation, “Intense coherent Cherenkov radiation due to the interaction of a relativistic electron bveam with a slow-wave structure,” Phys. Rev. Lett., vol. 33, 21 pp. 1278-1282, Nov. 1974.

[2] N. F. Kovalev, M. I. Petelin, M. D. Raizer, A. V. Smorgonskii, and L. E. Tsopp, “Generation of powerful electromagnetic radiation pulses by a beam of relativistic electrons,” JETP Lett., vol. 18, pp. 138-140, 1973.

[3] Y. Carmel, H. Guo, W. R. Lou, D. Abe, V. L. Granatstein, and W. W. Destier, “Novel method for determining the electromagnetic dispersion relation of periodic slow wave structures,” Appl. Phys. Lett., vol. 51, 13, pp. 1304-1306, Sep. 1990.

[4] A. V. Gunin, A. I. Klimov, S. D. Korovin, I. K. Kurkan, I. V. Pegel, S. D. Polevin, A. M. Roitman, V. V. Rostov, A. S. Stepchenko, and E. M. Totmeninov, “Relativistic X-band BWO with 3-GW output power,” IEEE Trans. Plasma Sci., vol. 26, no. 3, pp. 326–331, Jun. 1998.

[5] S. J. Smith, and E. M. Purcell, “Visible light from localized surface charges moving across a grating,” Phys. Rev., vol. 92, pp. 1069, 1953.

[6] J. Urata, M. Goldstein, M. F. Kimmitt, A. Naumov, C. Platt, and J. E. Walsh, “Superradiant Smith-Purcell emission,” Phy. Rev. Lett., vol. 80, no. 3, pp. 516-519, Jan. 1998.

[7] H. L. Andrews, C. H. Boulware, C. A. Brau, and J. D. Jarvis, “Dispersion and attenuation in a Smith-Purcell free electron laser,” Phys. Rev. ST Accel. Beams, vol. 8, 050703, May 2005.

[8] H. L. Andrews, C. A. Brau, J. D. Jarvis, C. F. Guertin, A. O’Donnell, B. Durant, T. H. Lowell, and R. R. Mross, “Observation of THz evanescent

waves in a Smith-Purcell free-electron laser," Phys. Rev. ST Accel. Beams, vol. 12, 080703, Aug. 2009.

[9] O. Watanabe, T. Watanabe, K. Ogura, T. Imai, and T. Cho, "Numerical study of electromagnetic surface wave on corrugated metal surface," Plasma Fusion Res., vol. 1, pp. 025-1-2, 2006.

[10] K. Ogura, K. Minami, M. M. Ali, Y. Kan, T. Nomura, Y. Aiba, A. Sugawara, and T. Watanabe, " Analysis on field lines and Poynting vectors in in corrugated wall waveguides," J. Phys. Soc., vol. 61, 11, pp. 3966-3976, Nov. 1992.

[11] B. Levush, T. Antonsen, Jr. A. Bromborsky, W. R. Lou, and Y. Camel, "Relativistic backward-wave oscillators: theory and experiment," Phys. Fluids, B 4, 2293, 1992.

[12] T. Watanabe, Y. Choyal, K. Minami, and V. L. Granatstein, "Range of validity of the Rayleigh hypothesis," Phys. Rev., E 69, 056606, 2004.

[13] K. Ogura, K. Komiyama, M. Sakai, D. Yamada, H. Saito, and H. Yamazaki, "Performance of weakly relativistic oversized backward wave oscillators," IEEJ Trans. Fundament. Mater., vol. 125, no. 9, pp. 733–738, 2005.

[14] S. Aoyama, Y. Miyazawa, K. Ogura, A. Sugawara, and M. Hirata, "Improved performance of oversized backward wave oscillator driven by weakly relativistic electron beam," Fusion Sci. Tech., vol. 51, no. 2T, pp. 325-327, Feb. 2007.

[15] K. Ogura, Y. Miyazawa, S. Aoyama, Y. Takamura, S. Tamura, and A. Sugawara, "Studies of a weakly relativistic oversized backward wave oscillator with disk cathode and rectangular corrugation," IEEJ Trans. Fundam. Mater., vol. 127, no. 11, pp. 681–686, Nov. 2007.

[16] Y. Takamura, Y. Kazahari, H. Oe, K. Ogura, A. Sugawara, and M. Hirata, "Operation characteristics of microwave sources based on slow-wave interactions in rectangular corrugations," Plasma Fusion Res., vol. 3, pp. S1078-1-5, Mar. 2008.

[17] Y. Takashima, K. Ogura, M. Yamakawa, K. Otubo, and Md. R. Amin, "Analysis of slow-wave instability in rectangularly corrugated cylindrical waveguide," J. Plasma Fusion Res. SERIES, vol. 8, pp. 1512-1517, 2009.

[18] K. Ogura, K. Yambe, K. Yamamoto and Y. Kobari, "Normal modes and slow-wave instabilities in oversized coaxial slow-wave structure with rectangular corrugations," IEEE Trans. Plasma Sci., vol. 41, no. 10, pp. 2729-2734, Oct. 2013.

[19] K. Ogura, A. Shirai, M. Ogata, S. Gong, and K. Yambe, "Beam interactions with surface waves and higher order modes in oversized G-band slow-wave structure," IEEE Trans. Plasma Sci., vol. 44, no. 2, pp. 201-210, Feb. 2016.

[20] H. Oe, K. Ogura, Y. Kazahari, K. Bansho, H. Iizuka, A. Sugawara, and W. S. Kim, "Experimental study on disk type cold cathode in weakly relativistic energy region," J. Plasma Fusion Res. SERIES, vol. 8, pp. 1477-1482, 2009.

[21] K. Yambe, K. Ogura, S. Hasegawa, T. Shinada, T. Iwasaki, and T. Furuichi, "Experimental study on generation of electron beam utilizing cold cathode in the weakly relativistic energy beam," IEEE Trans. Plasma Sci., vol 41, 10, pp. 2781-2785, Oct. 2013.

[22] D. M. Pozar, *Microwave Engineering*, 4th ed. New York, NY, USA: Wiley, (2012), p. 720.

Chapter 3

Experimental Study for Terahertz Radiations

3.1. Introduction

Experimental devices used in the laboratory, experimental set-up and operation are presented in Section 2.5 and 2.6. Experimental studies of the K-, Q-, and G-band oversized BWOs of the laboratory at Niigata University are presented in [1]-[3]. Relation of power and frequency of high power microwave devices; solid state devices (avg), vacuum devices (avg), and vacuum HPM (peak), are summarized and depicted in Ref. [4]. The previous works of the laboratory stand in the upper region of the vacuum devices (avg), shown in Fig. 1.2. Experimental studies for surface-wave oscillator with upper cutoff frequency of 0.1 THz mentioned as SWO (0.1 THz), and surface-wave resonator with upper cutoff frequency of 0.35 THz and 0.5 THz mentioned as SWRs (0.35 THz) and (0.5 THz) are presented in this chapter. The parameters of the SWS for each type are shown in Table 2.4. Major difference among them is that the corrugation amplitude h of the SWO (0.1 THz) is two (four) times larger than that of the SWRs (0.35 THz) and (0.5 THz). Experiments are carried out for each type by varying the length of the SWS.

In Sections 3.2, 3.3, and 3.4, experimental and numerical results of the SWO (0.1 THz), SWR (0.35 THz), and SWR (0.5 THz) are presented, respectively. In Section 3.5, figure of merits of each type are presented. Summary and conclusion are presented in Section 3.6.

3.2. Surface-wave Oscillator with Upper Cutoff Frequency of 0.1 THz

Parameters of the SWS with the upper cutoff frequency of 0.1 THz are shown in Table 2.4. A sectional photograph of the SWS taken by a microscope is shown in Fig. 3.1(a). The diameter of the SWS D_s is approximately ten times larger than the free-space wavelength of the output electromagnetic wave λ: where λ is approximately 0.3 cm. In the experiment, the cathode with diameter of 29 mm is used. The radiated signals are picked up by F- and G-band horn antennas, which are EIA standard rectangular waveguides with cutoff frequencies of 74 and 116 GHz, respectively [5]. Various lengths of the SWS; $20z_0$, $40z_0$, $80z_0$, and $120z_0$ which two modules of SWSs are combined, are examined. The dispersion relation of the SWS, which is presented in the following section, has potential of a SWO presented in Section 4.2, and the SWS is mentioned as SWO (0.1 THz).

3.2.1. Dispersion relation of the SWO (0.1 THz)

Dispersion relation of the SWO (0.1 THz) shown in Fig. 3.2 is obtained by equation (2.6). The fundament TM_{01} mode is periodic in wave number space (k_z-space) with a period of k_0 = 125.66 cm^{-1}, and has an upper cutoff frequency of approximately 0.1 THz. By the group velocity of the dispersion relation, three regions are assigned as follows; TWT region where the positive group velocity is, BWO region where the negative group velocity is, and π-point where $k_z = k_0/2$ = 62.8 cm^{-1} and the group velocity of the dispersion relation vanishes. As references, electron beam energy lines of 15, 32.5, and 80 keV are depicted in the figure to predict the operation regions. At low electron beam line of less than 32.5 keV, the interaction of the beam line and dispersion relation is in the BWO region. At high electron beam line of greater than 32.5 keV, the interaction is in the TWT region. At the intermediate beam line approximately 32.5 keV, the interaction is at the π-point or the Bragg condition. The overall operation from the BWO to TWT has been studied theoretically, and it has been shown that there is no operation near the

π-point [6]. To date, the theoretical prediction has not been validated against experimental results.

3.2.2. Experimental results of the SWO (0.1 THz)

Typical waveforms of the measured signals for the SWO (0.1 THz) with the SWS of $40z_0$ are shown in Fig. 3.3. The detected signal is obtained by F-band (90–140 GHz) horn antenna with 10 dB attenuation, and G-band (140–220 GHz) horn antenna with 0 dB attenuation, at a position of 600 mm away from the output window. In the experiment, meaningful radiations are detected by F-band antenna, and not by G-band antenna. And detected powers are evaluated by using F-band detected voltage signals, which are calibrated to absolute powers by using a Gunn oscillator at 0.1 THz. Detected powers and beam currents versus beam voltages of the SWO are shown in Fig. 3.4.

Figure 3.4(a) is experimental results for the SWS of $20z_0$. Meaningful radiation is started when the beam voltage of approximately 25 kV, and the radiation region is up to 55 kV. The peak detected power is approximately 1100 mW when the beam voltage of approximately 42 kV. When the length of the SWS is increased to 40 periods, the radiation region is from the beam voltage of approximately 10 to 85 kV, shown in Fig. 3.4(b). By increasing the beam voltage, the radiation power is increased, and the peak detected power is approximately 10 W when the beam voltage is approximately 80 kV. The SWO with the SWS of both $20z_0$ and $40z_0$ operates in all regions; BWO, π-point and TWT regions, as the radiations occur from beam voltage of less than 32.5 kV to large than that, as shown in Fig. 3.2.

Experimental results of the SWO with the SWS length of 80 and $120z_0$ are shown in Fig. 3.4(c) and (d), respectively. Both have the same radiation starting beam voltage of approximately 10 kV, and meaningful radiation disappears when the beam voltage of approximately 25 kV. No meaningful radiation is around the beam voltage of 32.5 kV for the SWS of $120z_0$, but incoherent radiations are

detected around that voltage for the SWS of $80z_0$. When the beam voltage is approximately 40 kV, meaningful radiations are detected again until the beam voltage of up to 85 kV. The peak detected power is approximately 10 W for the SWS of $80z_0$ when the beam voltage is in the range of 65 to 85 kV, and 20 W for the SWS of $120z_0$ when the beam voltage is approximately 80 kV. The operating regions of the SWO with the SWS of both 80 and $120z_0$ are in the BWO and TWT regions, and not around the π-point.

In order to examine the operating mode, radiation patterns are obtained by moving a receiving horn antenna in an equatorial plane around a pivot at the center of the output window. The horizontal components of the electric field are measured. The radiation pattern for the TWT operation with the SWS of $80z_0$, the BWO operation with the SWS of $40z_0$, and the π-point operation with the SWS of $40z_0$ are shown in Fig. 3.5(a), (b), and (c), respectively. As references, theoretical radiation curves for the TM_{01}, TM_{02}, TM_{03}, and TM_{04} waveguide mode are depicted in the figures. For the TWT and BWO operations, the measured patterns appear to be axisymmetric with a dip at the center. The patterns are broad and cannot be explained by a single TM_{01} mode. Higher order waveguide modes are required to explain these broad radiations. For the π-point operation, the radiation pattern approaches the TM_{01} mode.

3.3. Surface-wave Resonator with Upper Cutoff Frequency of 0.35 THz

Parameters of the SWS with upper cutoff frequency of 0.35 THz are shown in Table 2.4. A sectional photograph of the SWS taken by a microscope is shown in Fig. 3.1(b). The diameter of the SWS D_s is approximately 30 times larger than the free-space wavelength of the output electromagnetic wave λ: where λ is approximately 0.1 cm. In the experiment, two cathodes with diameter of 29 and 29.5 mm are used. The radiated signals are picked up by the H-band horn antenna connected with WR-3 waveguide, which are EIA standard rectangular waveguide

with cutoff frequency of 0.173 THz. High pass filters (HPFs) of 0.27 and 0.3 THz are used to confirm the radiated frequencies. Various lengths of the SWS; $40z_0$, $60z_0$, $80z_0$, and $120z_0$ which two modules of SWSs are combined, are examined. The dispersion relation of the SWS, which is presented in the following section, has potential of a SWR presented in Section 4.2, and the SWS is mentioned as SWR (0.35 THz).

3.3.1. Dispersion relation of the SWR (0.35 THz)

The dispersion relation of the SWR is obtained by equation (2.6) and shown in Fig. 3.6. The fundament TM_{01} mode is periodic in wave number space (k_z-space) with a period of k_0 = 251.32 cm^{-1}, and has an upper cutoff frequency of approximately 0.35 THz. The dispersion relation of the SWR is relatively steeper than that of the SWO (0.1 THz) as the length of the corrugation amplitude of the SWR is two times less than that of the SWO. In the figure, a light line is plotted as a reference to divide the dispersion relation into two regions; Region-I where the dispersion relation diverges from the light line, and Region-II where the dispersion relation closes to the light line. The regions are assigned by the group velocity related to the velocity of light, which are presented in Section 5.2. The electron beam lines of 23, 32, 40, and 80 keV are inserted in the figure, and all intersect the dispersion curve in Region-I. When the beam line is much less than 23 keV, the intersection of the beam line approaches to the boundary of Region-I and Region-II.

3.3.2. Experimental results of the SWR (0.35 THz)

Typical waveforms of the measured signals for the SWR with the SWS of $80z_0$ are shown in Fig. 3.7. The cathode with diameter of 29 mm is used for the SWS of 60, 80, and $120z_0$. The detected powers and beam currents versus beam voltages for the SWS of $80z_0$ are shown in Fig. 3.8(a). The meaningful radiations are detected with the beam voltages from approximately 32 up to 80 kV. The peak detected power is of approximately 85 mW when the beam voltage is of 45 kV. By the dispersion relation shown in Fig. 3.6, the beam line of 32 keV (40 keV)

intersects the dispersion curve at the frequency of approximately 0.27 THz (0.3 THz). In the experiment, the detected signals are confirmed by using HPFs of 0.27 and 0.3 THz. By the agreement of the numerical and experimental results, the radiated frequency region can be defined from 0.27 to 0.34 THz with the beam energy of 32 and 80 keV, respectively.

The detected powers and beam currents versus beam voltages for the SWS of 60 and $120z_0$ are shown in Fig. 3.8(b). Meaningful radiations are detected starting at the beam voltage of approximately 42 kV (23 kV) for the SWS of $60z_0$ ($120z_0$). The peak detected power is of approximately 110 mW for both conditions. By the dispersion relation shown in Fig. 3.6, the radiation frequency is of approximately 0.26 THz at the intersection of the beam line of 23 keV with the dispersion curve. No meaningful radiation is observed for the SWS of $40z_0$ even with the beam voltage increasing up to approximately 90 kV. By increasing the diameter of the cathode from 29 to 29.5 mm, meaningful radiation is started at the beam voltage of approximately 40 kV for the SWS of $40z_0$, and the peak detected power is approximately 110 mW, shown in Fig. 3.8(b).

A broad radiation pattern of the oscillator for the SWS of $80z_0$ is obtained when the beam voltage and beam current are of approximately 50 kV and 400 A, shown in Fig. 3.9. The radiation pattern is broad and higher order waveguide modes are required to explain the radiation pattern.

3.4. Surface-wave Resonator with Upper Cutoff Frequency of 0.5 THz

Parameters of the SWS with upper cutoff frequency of 0.5 THz are shown in Table 2.4. A sectional photograph of the SWS taken by a microscope is shown in Fig. 3.1(c). The diameter of the SWS D_s is approximately 40 times larger than the free-space wavelength of the output electromagnetic wave λ: where λ is approximately 0.075 cm. In the experiment, the cathode with diameter of 29 mm is used. The radiated signals are picked up by the H-band horn antenna connected

with WR-3 waveguide. High pass filters (HPFs) of 0.35 and 0.4 THz are used to confirm the radiated frequencies. Various lengths of the SWS; $120z_0$, $160z_0$, $320z_0$, and $400z_0$, are examined. Two modules of SWSs for $120z_0$ and $320z_0$, and three modules for $400z_0$ are combined. The dispersion relation of the SWS, which is presented in the following section, has potential of a SWR presented in Section 4.2, and the SWS is mentioned as SWR (0.5 THz).

3.4.1. Dispersion relation of the SWR (0.5 THz)

Dispersion relation of the SWR by equation (2.6) is shown in Fig. 3.10. The fundament TM_{01} mode is periodic in wave number space (k_z-space) with a period of $k_0 = 251.32$ cm^{-1}, and has an upper cutoff frequency of approximately 0.5 THz. The dispersion relation of the SWR is relatively steeper than that of the SWR (0.35 THz) as the length of the corrugation amplitude of the SWR is two times less than that of the SWR (0.35 THz). Decreasing the length of the corrugation amplitude in 50% is increasing the upper cutoff frequency by approximately 43%. In the figure, a light line and the electron beam lines of 32 and 80 keV are inserted. The intersections of the electron beam lines with the dispersion curve are in Region-I. When a beam line is less than 32 keV, the intersection approaches to Region-II.

3.4.2. Experimental results of the SWR (0.5 THz)

Typical waveforms of the measured signals for the SWR with the SWS of $160z_0$ are shown in Fig. 3.11. The detected powers and beam currents versus beam voltages for the SWS of 120, 160, 320, and $400z_0$ are shown in Fig. 3.12. Meaningful radiation is started when the beam voltage of 75 kV, 40 kV and 35 kV for the SWS of $120z_0$, $160z_0$ and $320z_0$, respectively. The radiation region is the beam voltage of approximately 35–80 kV, and by the dispersion relation, the radiation frequency range for the beam voltages is approximately 0.31–0.4 THz. In the experiment, the radiated frequency is detected by HPF of 0.35 THz, and no radiation is confirmed by HPF of 0.4 THz at the beam voltage of approximately 80 kV. The radiation starting beam voltage is a decreasing function of the length of the

SWS of up to $320z_0$. Even though the length of the SWS is increased to $400z_0$, the radiation starting voltage is not decreased properly and standstills at approximately 32 kV, shown in the figure. The peak detected power is of approximately 800 mW.

3.5. Figure of Merits

Figure of merit Pf^2 is the performance of the oscillator; where P is the radiated power, and f is the operating frequency. For the previous studied for the X-, K-, Q-, and G-band oversized BWOs, the figure of merit is approximately 3.5×10^2 MW.GHz^2 [1], [7], [3], as shown in Fig. 3.13.

For the SWO (0.1 THz), the peak detected power of approximately 20 W and the broad radiation pattern are observed in the TWT region, as shown in Fig. 3.4(d) and 3.5(a). By integrating the peak detected power over the broad radiation pattern, the corresponding maximum radiation power is estimated to be approximately 20 kW. And the figure of merit is approximately 2×10^2 MW.GHz^2. For the SWR (0.35 THz), by integrating the peak detected power of approximately 110 mW which corresponds to approximately 0.285 kW over the radiation pattern, the figure of merit is approximately 0.26×10^2 MW.GHz^2. No radiation pattern for the SWR (0.5 THz) is experimentally studied. And an assumption is made that the radiation pattern of the SWR (0.5 THz) may be nearly the same pattern of the SWR (0.35 THz) as both SWSs have the same parameters expect the corrugation amplitude. The peak detected power of the SWR (0.5 THz) is approximately 800 mW which corresponds to approximately 2.6 kW, and the figure of merit can be estimated approximately 4×10^2 MW.GHz^2.

3.6. Summary and Conclusion

The SWO (0.1 THz) can be mentioned as a W-band oscillator as its cutoff frequency is approximately 0.1 THz. By varying the length of the SWS and the

beam energy, the SWO operates in different regions. At the beam energy of lower and higher than 32.5 keV, the operation regions are in the BWO and TWT regions. When the length of the SWS is relatively short, the SWO operates in all regions; BWO, π-point, and TWT regions. For longer length of the SWS, the π-point operation disappears. The detected power is an increasing function of the length of the SWS. In the BWO and TWT regions, the SWO is found to be a multimode system, and many modes may be excited simultaneously. Around the π-point operation, the higher order modes in the multimode system are suppressed and the oscillation approaches a single mode operation.

For the SWR (0.35 THz), the radiation starting beam voltage is getting low as the length of the SWS is longer. A broadband radiation of approximately 0.1 THz can be tuned by the beam voltage of less than 80 kV. The operation region is still in Region-I even though the beam energy is of approximately 23 keV, and meaningful radiation can be expected for the beam energy of less than 23 keV as shown in Fig. 3.6. By the dispersion relations of the SWR, the group velocity of the SWR (0.35 THz) is relatively less than that of the SWR (0.5 THz); which is described in Chapter 5. Consequently, more intense radiations by the SWR (0.35 THz) rather than the SWR (0.5 THz) can be theoretically expected. But the experiment results show that the peak detected power of the SWR (0.35 THz) is relatively lower than that of the SWR (0.5 THz). One of the possible reasons is that the external magnetic field alignment is not good enough to confirm the electron beam flowing in the axial direction during the experiment of the SWR (0.35 THz).

For the SWR (0.5 THz), a broadband radiation of approximately 0.1 THz is detected by the beam voltage of less than 80 kV. The radiation starting beam voltage is the decreasing function of the length of the SWS until the intersection of the beam line and dispersion curve is in Region-I. When the intersection approaches into Region-II, even though the length of the SWS is increased, the radiation starting beam voltage could not be reduced.

(a) (b) (c)

Fig. 3.1 Cross sectional photograph of (a) SWO (0.1 THz), (b) SWR (0.35 THz), and (c) SWR (0.5 THz) taken by a digital microscope.

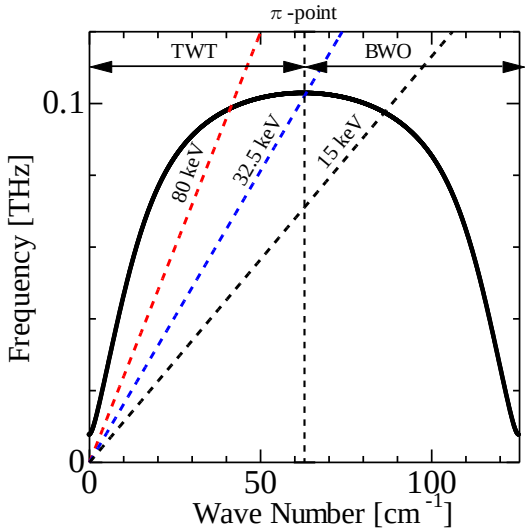

Fig. 3.2 Dispersion relation of the SWS for the SWO (0.1 THz).

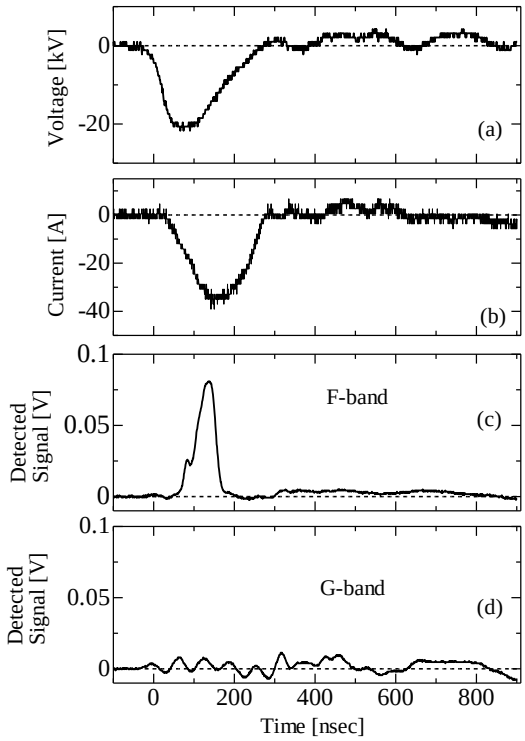

Fig. 3.3 Waveforms of the measured signals of the SWO (0.1 THz): (a) beam voltage, (b) beam current, (c) detected signal by F-band antenna when the beam voltage and current of 15.23 kV and 32.87 A, and (d) detected signal by G-band antenna.

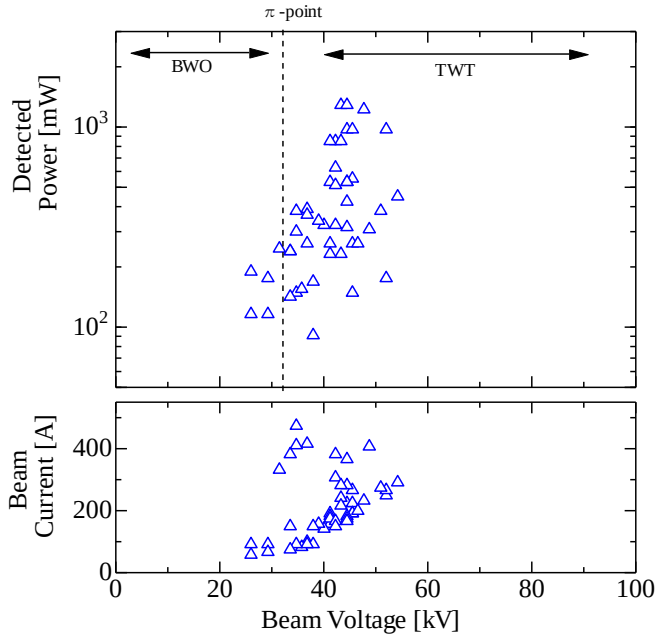

(a)

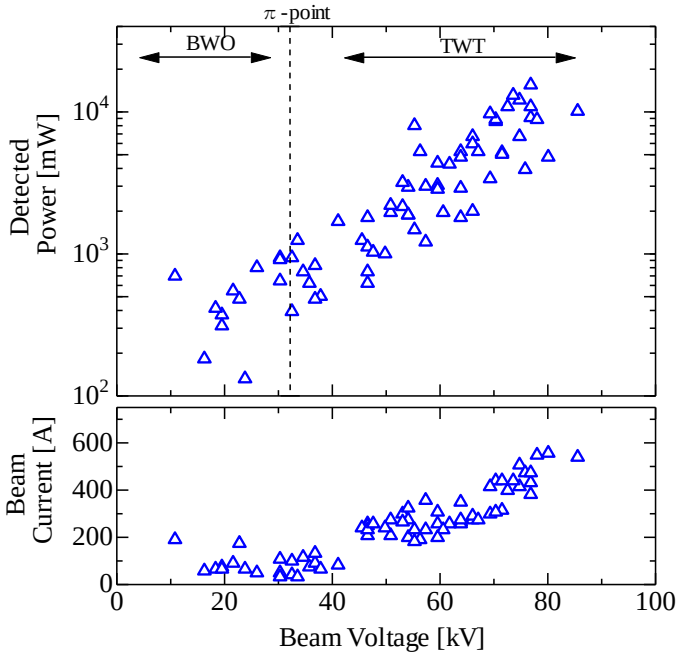

(b)

Fig. 3.4 SWO (0.1 THz): Peak value signals and beam current versus beam voltage for the SWS length of (a) $20z_0$, and (b) $40z_0$. The beam voltages at the radiation peaks are used. The magnetic field is approximately 0.82 T. (Reproduced from Ref. [8])

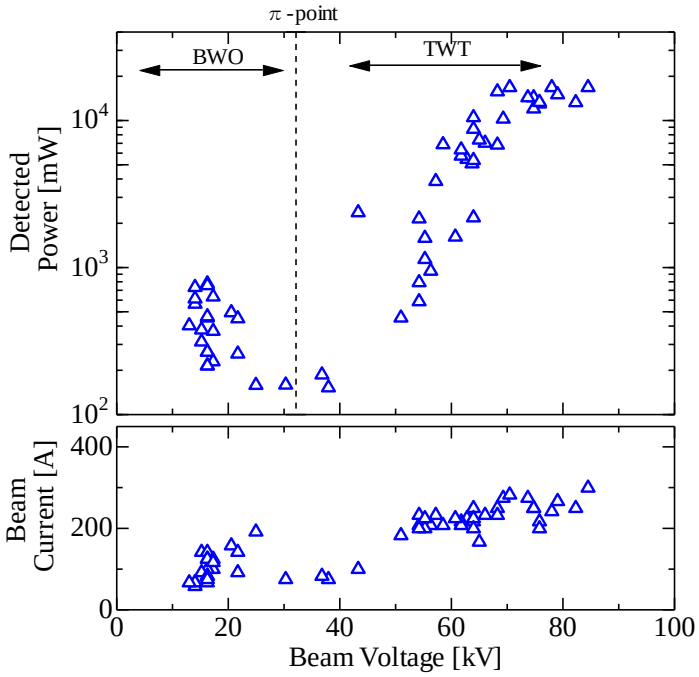

(c)

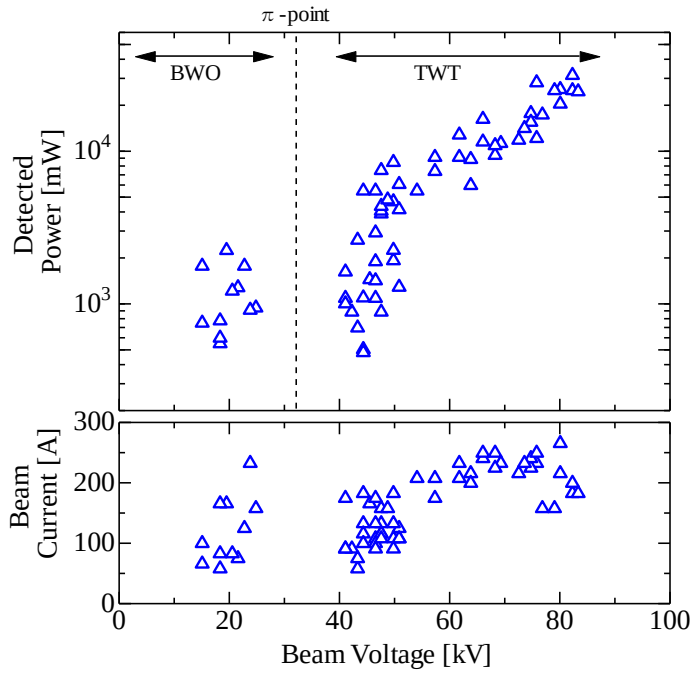

(d)

Fig. 3.4 SWO (0.1 THz): Peak value signals and beam current versus beam voltage for the SWS length of (c) $80z_0$ and (d) $120z_0$. The beam voltages at the radiation peaks are used. The magnetic field is approximately 0.82 T. (Reproduced from Ref. [8])

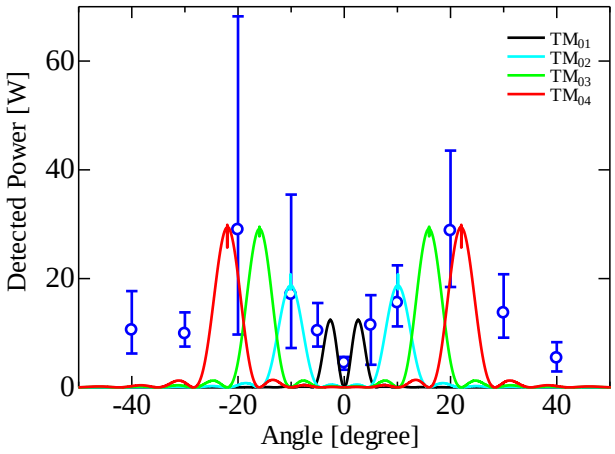

(a)

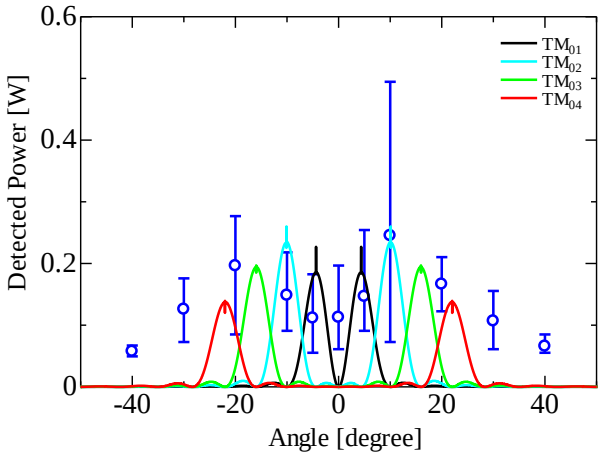

(b)

Fig. 3.5 SWO (0.1 THz): (a) Radiation pattern for the TWT operation with the SWS length of $80z_0$. The operating parameters are approximately 70 kV, 200 A and 0.82 T. (b) Radiation pattern for the BWO operation with the SWS of $40z_0$. The operating parameters are approximately 20 kV, 60 A and 0.82 T. The solid curves are the calculated radiation pattern for the TM_{01}, TM_{02}, TM_{03}, and TM_{04} waveguide mode.

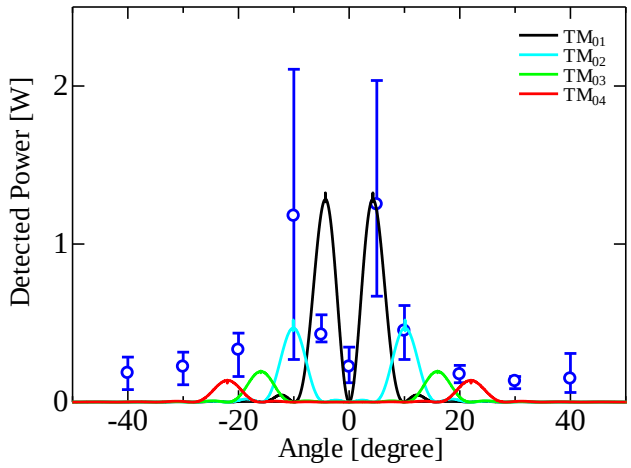

(c)

Fig. 3.5 SWO (0.1 THz): (c) Radiation pattern for the π-point operation of the SWS length of $40z_0$. The operating parameters are approximately 30 kV, 150 A and 0.82 T. The solid curves are the calculated radiation pattern for the TM_{01}, TM_{02}, TM_{03}, and TM_{04} waveguide mode.

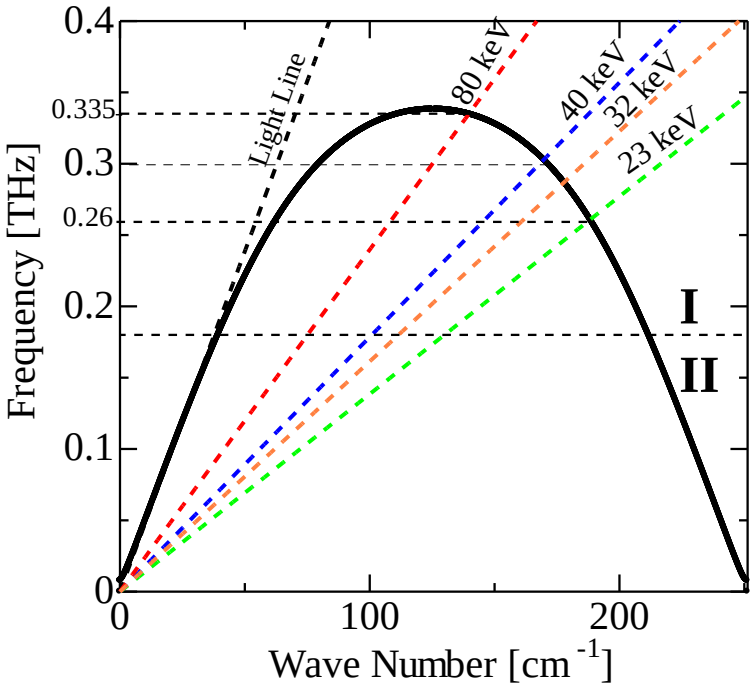

Fig. 3.6 Dispersion relation of the SWS for the SWR (0.35 THz).

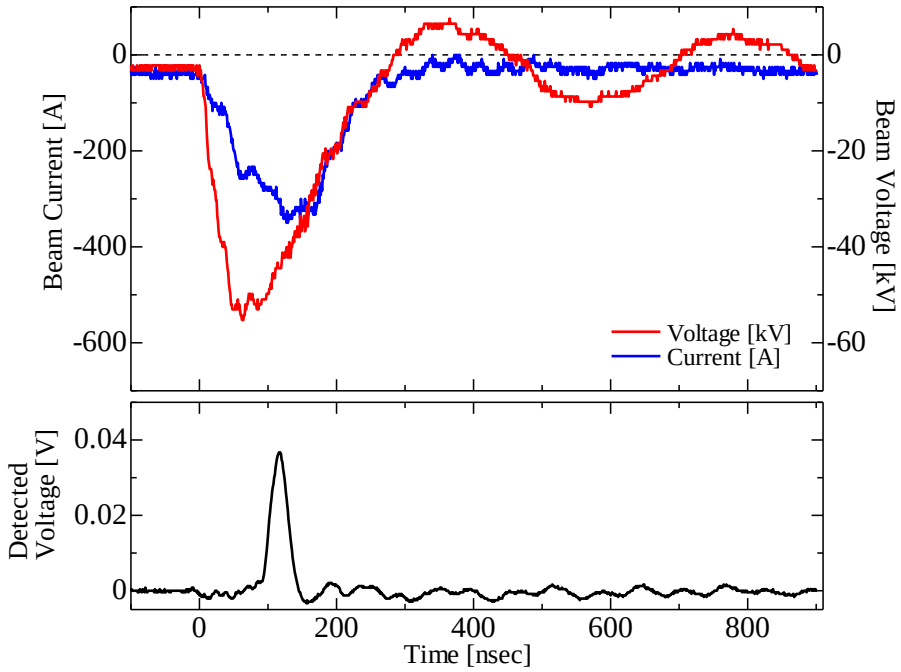

Fig. 3.7 Waveforms of the measured signals for the SWR (0.35 THz) with the SWS length of $80z_0$: the beam voltage, the beam current, and the detected signal. The peak signal is detected when the beam voltage and the beam current of 45 kV and 308 A.

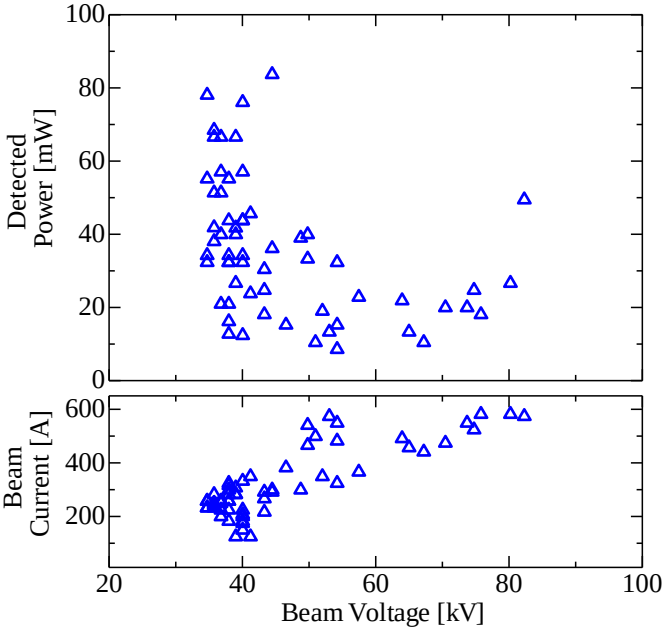

(a)

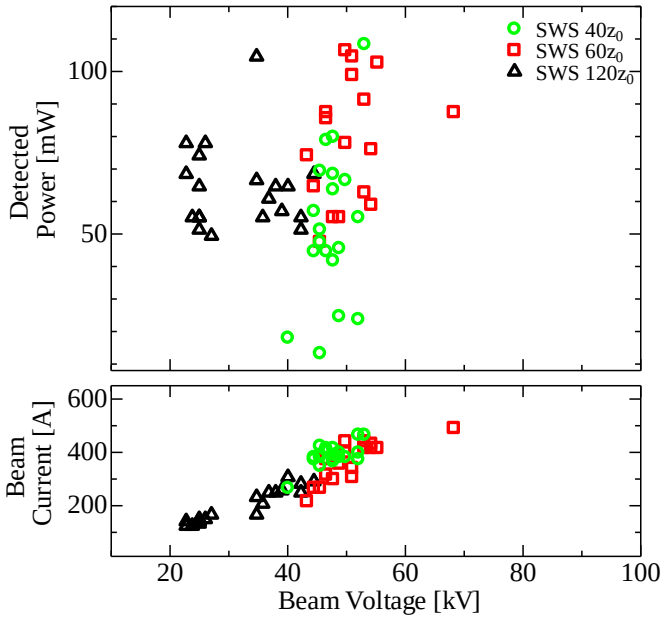

(b)

Fig. 3.8 SWR (0.35 THz): Peak value signals and beam current versus beam voltage for the SWS length of (a) 80, (b) 40, 60, and 120z_0. Data with the SWS length of 40z_0 are obtained by incresing the cathode daiameter from 29 mm to 29.5 mm. The beam voltages at the radiation peaks are used. The magnetic field is approximately 0.82 T. (Reproduced from Ref. [9])

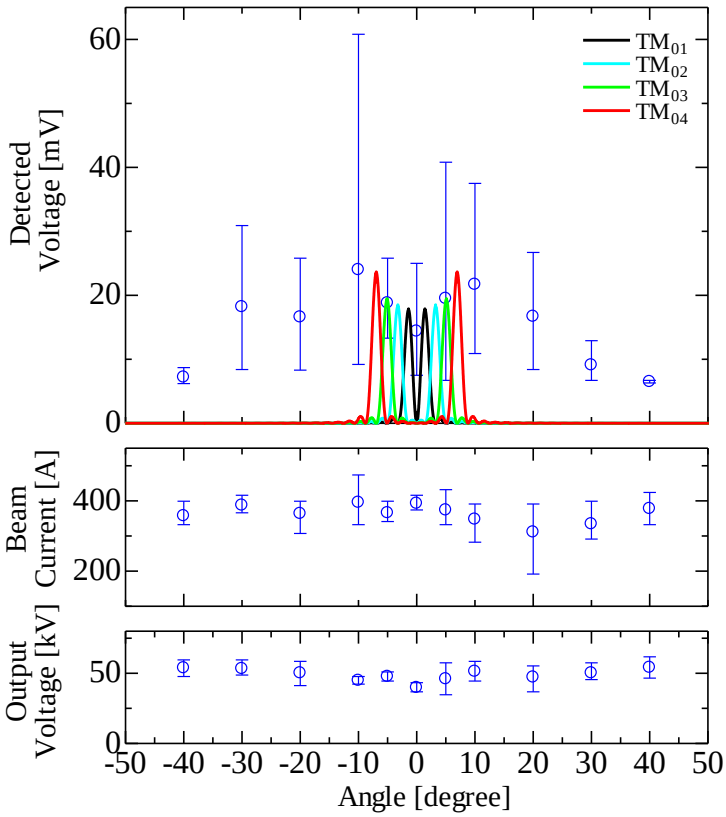

Fig. 3.9 SWR (0.35 THz): Radiation pattern of the SWS length of $80z_0$. The operating parameters are approximately 50 kV, 400 A and 0.82 T. The solid curves are the calculated radiation pattern for the TM_{01}, TM_{02}, TM_{03}, and TM_{04} waveguide mode.

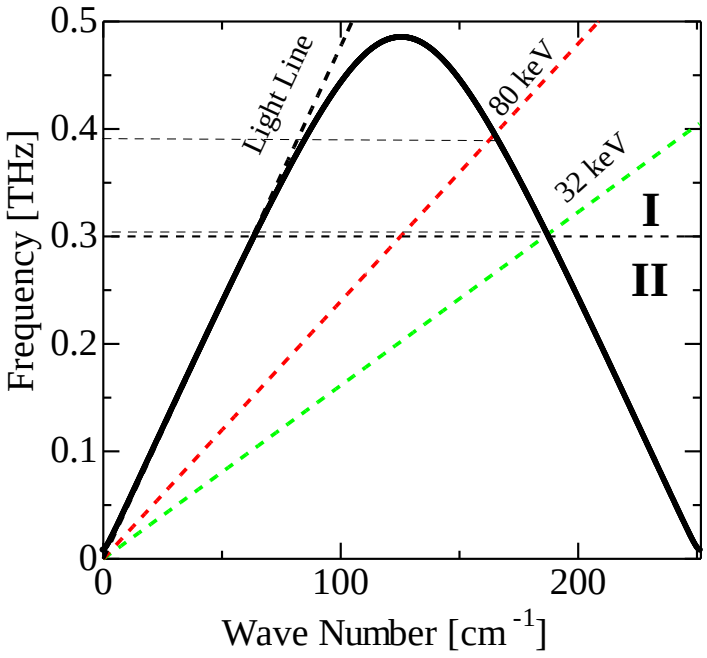

Fig. 3.10 Dispersion relation of the SWS for the SWR (0.5 THz).

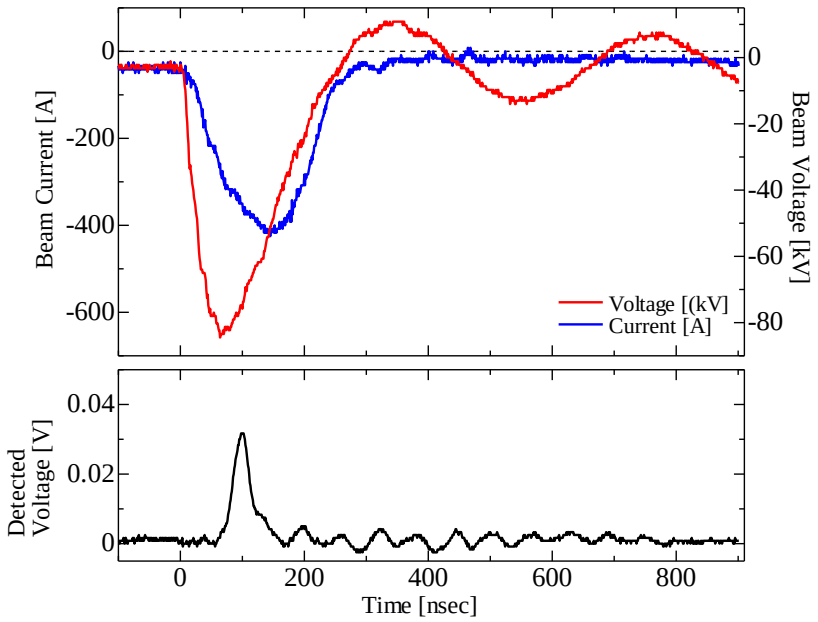

Fig. 3.11 Waveforms of the measured signals for the SWR (0.5 THz) with the SWS length of $160z_0$: the beam voltage, the beam current, and the detected. The peak signal is detected when the beam voltage and the beam current of 75 kV and 350 A.

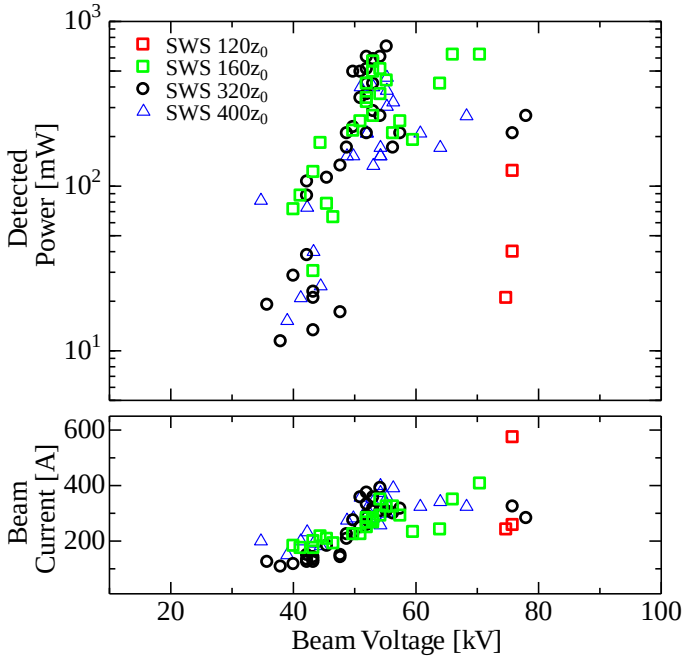

Fig. 3.12 SWR (0.5 THz): Peak value signals and beam current versus beam voltage for the SWS length of 120, 160, 320, and 400 z_0. The beam voltages at the radiation peaks are used. The magnetic field is approximately 0.82 T. (Reproduced from Ref. [9])

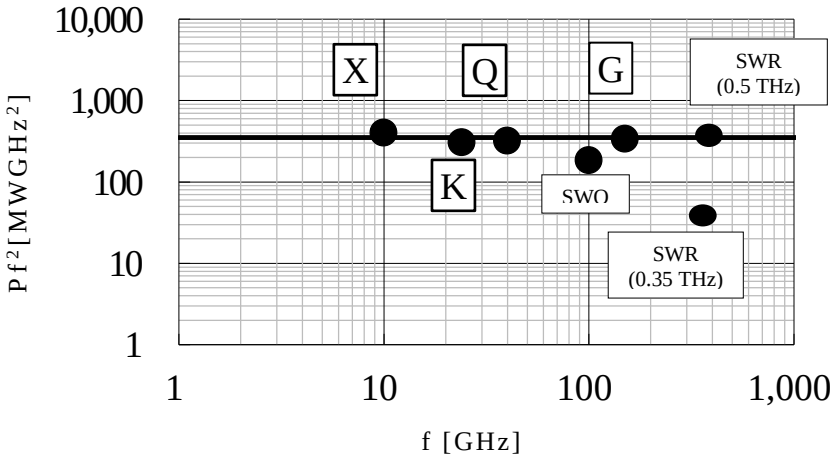

Fig. 3.13 Figure of merits of the X-, K-, Q- and G-band, SWO (0.1 THz), SWR (0.35 THz), and SWR (0.5 THz).

References

[1] S. Aoyama, Y. Miyazawa, K. Ogura, A. Sugawara, and M. Hirata, "Improved performance of oversized backward wave oscillator driven by weakly relativistic electron beam," Fusion Sci. Tech., vol. 51, no. 2T, pp. 325-327, Feb. 2007.

[2] K. Ogura, Y. Miyazawa, S. Aoyama, Y. Takamura, S. Tamura, and A. Sugawara, "Studies of a weakly relativistic oversized backward wave oscillator with disk cathode and rectangular corrugation," IEEJ Trans. FM, vol. 127, no. 11, pp. 681–686, Nov. 2007.

[3] S. Gong, K. Ogura, S. Nomizu, A. Shirai, K. Yamazaki, K. Yambe, S. Kubo, T. Shimozuma, S. Kobayashi, and K. Okada, "Oscillation starting conditions for oversized G-band (140 – 220 GHz) backward wave oscillator driven by weakly relativistic electron beam," IEEE Trans. Plasma Sci., vol. 43, no. 10, pp. 3530-3536, Oct. 2015.

[5] D. M. Pozar, *Microwave Engineering*, 4th ed. New York, NY, USA: Wiley, (2012), pp. 720.

[6] H. L. Andrews, C. H. Boulware, C. A. Brau, and J. D. Jarvis, "Dispersion and attenuation in a Smith-Purcell free electron laser," Phys. Rev. ST Accel. Beams vol. 8, 050703, May 2005.

[7] S. Magori, K. Ogura, T. Iwasaki, J. Kojima, K. Yambe, S. Kubo, T. Shimozuma, S. Kobayashi, and K. Okada, "Experimental study on G-band oversized backward wave oscillator driven by weakly relativistic electron beam," Plasma Fusion Res., vol. 9, 3406032, Apr. 2014.

[8] M. T. San, K. Ogura, K. Yambe, Y. Annaka, S. Gong, J. Kawamura, T. Miura, S. Kubo, T. Shimozuma, S. Kobayashi, and K. Okada, "Experimental study on W-band (75 – 110 GHz) oversized surface wave oscillator driven by weakly relativistic electron beams," Plasma Fusion Res., vol. 11, p. 2406085, Jun. 2016.

[9] M. T. San, K. Ogura, K. Kubota, Y. Annaka, K. Yambe, and A. Sugawara, “Study on Operation of Oversized Backward Wave Oscillator for Broadband Terahertz Radiation,” IEEE Trans. Plasma Sci., accepted for publication on Jan 11, 2018.

Chapter 4

Operation of a Surface-wave Oscillator around π-point Region

4.1 Introduction

The operation regions: TWT, π-point, and BWO, of an oscillator are loosely defined by a conventional dispersion relation, and the absolute instability occurs in the BWO region and the convective instability in the TWT region. But the conventional way to distinguish between the BWO and TWT region by referring a dispersion relation becomes insufficient and ambiguous when a practical instability arises at the intersection of the beam mode and structure wave mode because the beam existence modifies the dispersion relation and both the frequency and wave number become complex in unstable regions. An accurate way to distinguish between the BWO and TWT region is to calculate the saddle-point in the dispersion relation, following the procedure of the so-called the saddle-point analysis [1]. In Section 3.2, it is experimentally pointed out that the SWO (0.1 THz) with relatively short length of the SWS operates in all regions. Around the π-point region, the instability could not be determined by the experimental results. And in this chapter, the numerical studies of the real wave number analysis and saddle-point analysis are presented to analyze the Cherenkov instability of the SWO (0.1 THz) operating around the π-point region.

In Section 4.2, a surface-wave oscillator and surface-wave resonator are defined by the conventional dispersion relation. In Section 4.3, real wave number analysis method is described for the non-zero electron beam, and the beam modes

and structure modes are analyzed. Saddle-point analysis method is presented in Section 4.4, and the Cherenkov instability is checked out for the absolute or convective instability. In Section 4.5, the operation around the π-point of the surface-wave oscillator is studied by the experimental and numerical results. Summary and conclusion are presented in Section 4.6.

4.2 Surface-wave Oscillator Vs Surface-wave Resonator

Dispersion relations for various lengths of the corrugation amplitude are shown in Fig. 4.1(a), while other parameters of the SWS are same as the SWO (0.1 THz) shown in Table 2.4. In the figure, the bottom curve; Curve-I, is for h = 0.3 mm, the middle one; Curve-II is for h = 0.15 mm, and the upper one; Curve-III, is for h = 0.075 mm. Light lines are depicted as a reference, and all curves are in the slow-wave region of the isosceles triangle formed by $\omega = k_z c$, $\omega = -(k_z - k_0)c$, and ω = 0, in which the wave phase velocity is less than the velocity of light. The regions of TWT, π-point, and BWO are assigned in the figure as presented in Section 3.2.1. The beam lines of 32.5 keV, 110 keV, and 350 keV intersect each curve at the π-point. The upper cutoff frequency is a decreasing function of h. But when h is deeper, the separation between the light line and curves is greater, and then the group velocity of the curve is lower. The group velocity of each curve is presented in Fig. 4.1(b); in the bounded surface-wave region of each curve, Curve-I has the lowest group velocity and Curve-III has the highest value. In addition, Curve-I is relatively flat around the π-point region, and beam lines intersect the curve at nearly the same frequency range. Consequently, coherent radiation with a narrow frequency or a single frequency range can be expected with Curve-I. And the other two curves intersect with beam lines at different frequency range, and incoherent radiation with a wide range of frequencies can be predicted [2].

The dispersion relation of the SWO (0.1 THz) has the similar characteristics of Curve-I and is defined as a surface-wave oscillator (SWO). And the SWRs (0.35 THz) and (0.5 THz) are similar to other curves and defined as surface-wave resonators (SWRs).

4.3 Real Wave Number Analysis

The dispersion relations described in the previous sections are real number curves; pure TM_{01} modes, when the beam current is assumed to be zero. In the BWO region, the electron beam and the structure wave move in the opposite direction and absolute instability is expected to occur. In the TWT region, both move in the same direction and convective instability may be induced. Around the π-point region, the transition of the movement of electron beams is in opposite direction and the instability could not be predetermined by the dispersion relation without the electron beam.

With the electron beam, $D^{(Z-)}$ and $D^{(T+)}$ in equation (2.6) become non-zero matrices due to the transverse cyclotron perturbations in a finite B_0 and combine the TM and the TE modes. And hence, electromagnetic waves become hybrid modes even in axisymmetric cases. The letters EH and HE are often used to designate the hybrid modes. In this study, TM is dominant in the EH mode, and TE is dominant in the HE mode [3]. The lowest axisymmetric EH mode is called EH_{01}. In the magnetized beam, there are fast space charge (FSC) and slow space charge (SSC) modes, and fast cyclotron (FC) and slow cyclotron (SC) modes. The SSC mode is coupled to EH_{01} mode, leading to Cherenkov instability. And the SC mode interacts with EH_{01} mode at the location of anomalous Doppler resonance and slow cyclotron instability occurs. The slow cyclotron instability is much weaker than the Cherenkov instability [4].

In the experiment, the applied magnetic field is approximately 0.82 T, and the numerical study of the dispersion relation with the electron beam for the same magnetic field is shown in Fig. 4.2: the parameters of the SWS are same as the SWO (0.1 THz) described in Table 2.4. Beam and structure wave modes are presented in the figure, and the Cherenkov instability is well isolated from the slow cyclotron instability. In addition, there is no pronounced effect of the SC mode on the Cherenkov instability such as the merger or the suppression [3], [5], [6]. The numerical study focus on the Cherenkov instability, and to analyze the intersection region of the beam mode with EH_{01} mode in detail the magnetic field strength is set at 5 T in the study. And the agreement between using of the magnetic field of 0.82 and 5 T is remarkable for the study of the Cherenkov instability. For the reasons, the saddle-point analysis presented in Section 4.4 is carried out with the magnetic field of 0.82 T.

The real wave number analysis results for the Cherenkov instability with the magnetic field of 5 T is presented in Fig. 4.3 and 4.4. The dispersion relations are plotted assuming a real wave number and complex value of frequency. Figure 4.3(a) and (b) are for the beam energy of 32.5 keV, and 50 keV which is relatively closed to the π-point beam energy. In the figure, point *C* is the highest frequency of the unstable region for the beam mode, point *M* separates the SSC mode and the backward-EH_{01} mode on the imaginary (k_z) zero line, and the trajectory of *CM* is the beam mode: which are presented in Section 4.4. As the beam mode and the backward-EH_{01} mode merge at *M*, the Cherenkov instability may be of absolute instability, and the operations are in the BWO region for the beam energy of 32.5 and 50 keV; which are at the π-point and TWT regions by the conventional dispersion relation described in Fig. 3.2.

The Cherenkov instability for the beam energy of 60 and 80 keV; which are sufficiently higher than the π-point beam energy of 32.5 keV, are shown in Fig. 4.4(a) and (b), respectively. By the dispersion relation in Fig. 3.2, these beams

interaction region is far from the π-point toward the TWT region. In this case, point *M* disappears in the curves, and two double roots; which are denoted by *A* and *B* in the figures, exist with the zero-group velocity. Point *B* is at the π-point where the forward- and backward-EH_{01} are merged. Therefore the trajectory of *AB* is of the forward-EH_{01} mode; which can be clearly recognized by Fig. 4.4(b) for the higher beam energy of 80 keV. The trajectory of *CA* is similar to *CM* and is an SSC mode. And point *A* is a merged point of the beam mode and forward-EH_{01} mode. For these reasons, the Cherenkov instabilities may be convective instabilities for which a beam interaction happens in the TWT region where the electron beam and the structure wave move in the same direction.

By varying the beam energy, point *C* in both Fig. 4.3 and 4.4 is localized at the different wave number but has no remarkable effect on the frequency region.

4.4 Saddle-point Analysis

The numerical results by the saddle-point analysis applying the procedure in [7] are shown in Fig. 4.5: the parameters of the SWS are same as the SWO (0.1 THz) described in Table 2.4. The absolute instability is given by a double root of k for a complex $\omega = \omega_r + \omega_i$ with positive ω_i, which is formed by two roots coming from different halves of the complex k_z-plane. Here, ω_r and ω_i are the real and imaginary parts of the angular frequency. The root coming downward from the top of the figure is for the forwardly propagating beam modes, and the root coming upward from the bottom of the figure is for the backwardly propagating structure modes. The absolute instability arises at the saddle-point where two roots merge, and oscillation occurs spontaneously without any original source of signal or any feedback loop. In the figure, solid lines are the roots of equation (2.6) for constant ω_r by changing ω_i. The roots marked by *U* coming from the upper half of k_z-plane are of SSC modes, and the roots marked by *L* coming from the lower half of k_z-plane are backward-EH_{01} modes. A saddle-point denoted by a black diamond is a

point where two modes are merged. Point *C* is plotted by Fig. 4.4, which is presented in the previous section.

Figure 4.5(a) and (b) are the analysis results for the beam energy of 32.5 keV and 50 keV, respectively. Point *M* is located at a point where the SSC mode merges with the backward-EH_{01} mode, and point *C* can be considered as a SSC mode because located in the roots by *U*. Therefore, the segment of *CM*; which corresponds to the trajectory of *CM* shown in Fig. 4.3, can be recognized as a beam mode. The saddle-point for the beam energy of 32.5 keV; which corresponds to the π-point in Fig. 3.2, is on the k_z-plane with the oscillation frequency $\mathrm{Re}(\omega)/2\pi$ = 0.102297 THz, the oscillation wavenumber $\mathrm{Re}(k_z)$ = 69.3 cm^{-1}, and the spatial growth rate $|\mathrm{Im}(k_z)|$ = 5 cm^{-1}, shown in Fig. 4.5(a). For the beam energy of 50 keV which corresponds to the TWT region in Fig. 3.2, the SSC mode also merges with the backward-EH_{01} mode at the saddle-point, where the oscillation frequency $\mathrm{Re}(\omega)/2\pi$ = 0.102782 THz, the oscillation wavenumber $\mathrm{Re}(k_z)$ = 61.2 cm^{-1}, and the spatial growth rate $|\mathrm{Im}(k_z)|$ = 3.5 cm^{-1}, shown in Fig. 4.5(b). Therefore, the Cherenkov instability remains to be absolute one while the SWO operates in the π-point and TWT regions of Fig. 3.2.

In Fig. 4.5(c) for the beam energy of 60 keV, points *B* is located by Fig. 4.4, and point *M* disappears and no merged point between a beam mode and backward-EH_{01} mode. No saddle-point is presented in the k_z-plane. Consequently, the absolute instability disappears for the beam energy. And the Cherenkov instability is the convective instability, where SSC modes and backward-EH_{01} modes move in the same direction. Note that even though the trajectory of *CA* in Fig. 4.4 seems to be an EH_{01} mode deformed by the beam, it is of an SSC mode in the roots of *U*. Hence, the point *A* in the Fig. 4.4 is a double root formed by the SSC and forward-EH_{01} modes.

4.5 π-point Operation of the SWO (0.1 THz)

By the experimental and numerical results, the operation of SWO (0.1 THz) is in all regions: BWO, π-point, and TWT. The saddle-point analysis shows that the Cherenkov instability of the SWO is the absolute instability up to the beam energy of approximately 50 keV. By the experimental results of the SWO with the SWS of $20z_0$ shown in Fig. 3.4(a), the upper limit of the operating region is up to the beam voltage of approximately 55 kV. And a remarkable agreement is between the experimental and numerical results on the upper limit of the absolute instability. For the lower limit, one possible mechanism is the starting current, which decreases by increasing the beam energy up to the π-point. In accordance of the method presented in [8], it is estimated on the order of 10 A (0.01 A) at 20 keV (32.5 keV) and reasonably explains the lower limit in Fig. 3.4(a). Therefore, for an SWO with relatively short length of the SWS, the operation around the π-point region is attributed to the absolute instability.

In the experiment of the SWO, the shortest length of the SWS is of $20z_0$ (10 mm): approximately three times shorter than the waveguide diameter of 30.2 mm, and the longest one is $120z_0$ (60 mm): approximately two times longer than the waveguide diameter. By increasing the length of the SWS, the operation region is extended into both the lower and higher beam voltage regions. Figure 3.4(d): the experimental results of the SWO with the SWS of $120z_0$, shows that radiations are clearly detected for the beam voltages below 25 kV in the BWO region. This might be caused by a decrease in the starting current due to the increase of the length of the SWS. And oscillations are also observed above 60 kV in the TWT region. In the experimental set-up, no matching section is at the ends of the SWS, and reflections of surface wave may be strong. The surface waves near the ends of the SWS are diffracted not only in the longitudinal direction but also in the transverse direction [9]. The cylindrical SWS length of $20z_0$ is approximately three times of the wavelength λ of the radiating electromagnetic wave and may be short enough to

form the π-point radiation by the constructive superposition of the diffracted surface waves from both SWS ends. However, the SWS length of $120z_0$ in is approximately 18λ and may be sufficiently long and the π-point radiation cannot be formed.

4.6 Summary and Conclusion

The dispersion relation with a flat surface around the π-point has relatively slow group velocity and as a result, coherent radiation can be expected and the beam lines intersect the dispersion curve at a single frequency range. The dispersion curve of the SWO (0.1 THz) has the same characteristics of the above, and is defined as a surface-wave oscillator. The operation around the π-point of the SWO could not be recognized by the experimental results. Real wave number analysis method points out the beam modes and forward- and backward structure modes of the dispersion curve, and saddle-point analysis method divides the absolute and convective instability. And by the numerical methods, the Cherenkov instability for the operation around the π-point is recognized as the absolute instability.

The experimental results show that the SWO with relatively short length of the SWS operates around the π-point. By increasing the length of the SWS, the operation regions are extended to the BWO and TWT regions, and for relatively long length of the SWS, no radiation is around π-point. The physics of the π-point radiation could not be unknown yet, but one possible mechanism is due to the end effects of the SWS. When the length of the SWS is close to the wavelength of the radiated electromagnetic wave, more diffracted waves from both ends of the SWS overlap and the π-point radiation is formed.

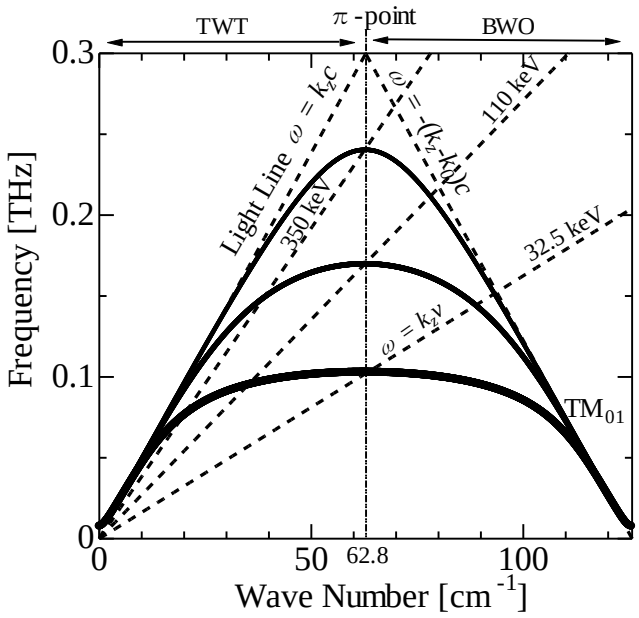

(a)

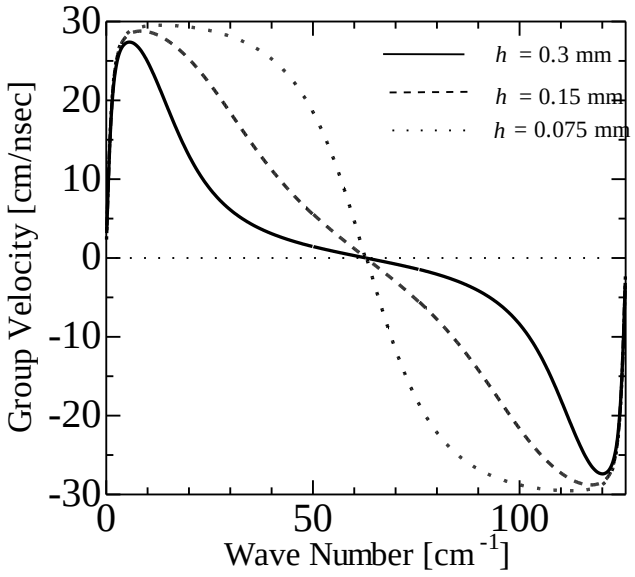

(b)

Fig. 4.1(a) Dispersion curve of TM_{01} mode based on the periodic scheme. Values of *h* are 0.075 mm (the uppermsot thin line), 0.15 mm (the middle thin line), and 0.3 mm (the thick solid line at the bottom), and other parameters are of the SWO (0.1 THz). Dotted lines are light lines and beams lines for 20, 32.5, and 50 keV. (b) Group velocity of (a).

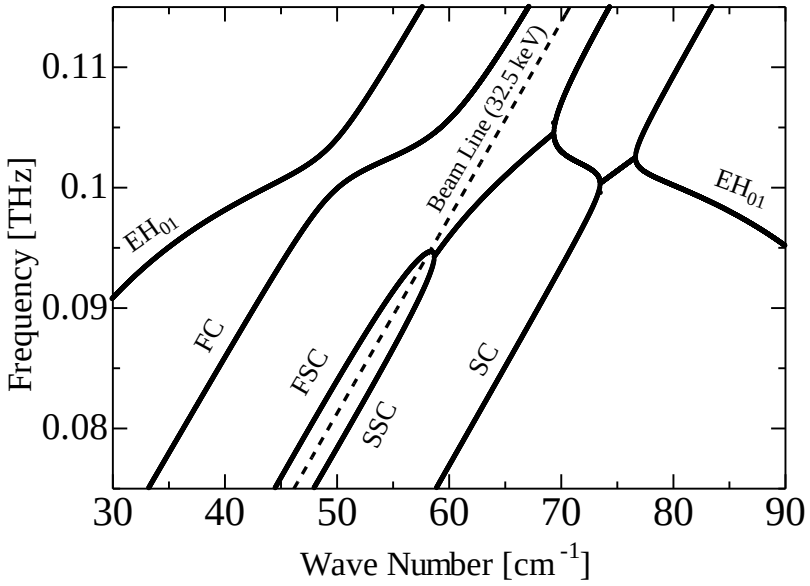

Fig. 4.2 Real frequncy for the EH_{01} mode, FSC and SSC modes, FC and SC modes with the external magnetic field B_0 = 0.82 T for the parameters of the SWO (0.1 THz). The beam energy and the beam current are 32.5 keV and 200 A.

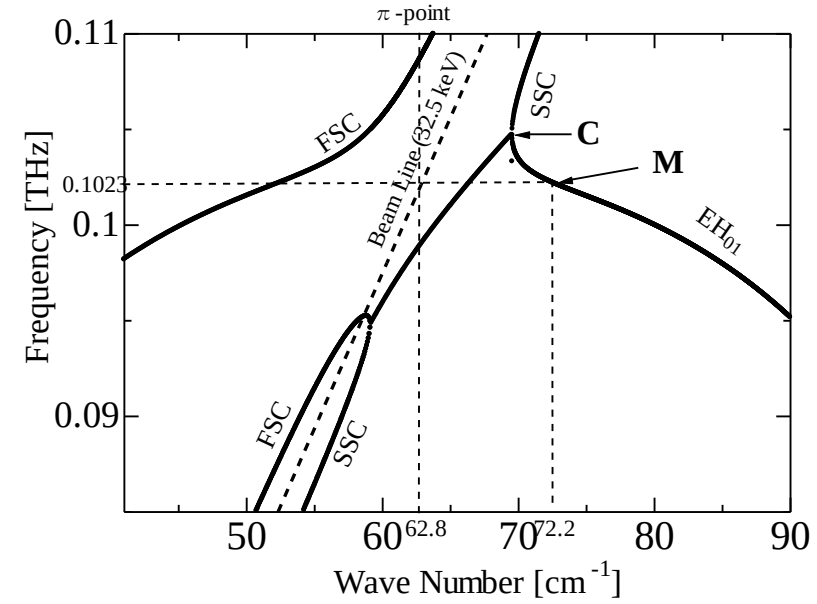

(a)

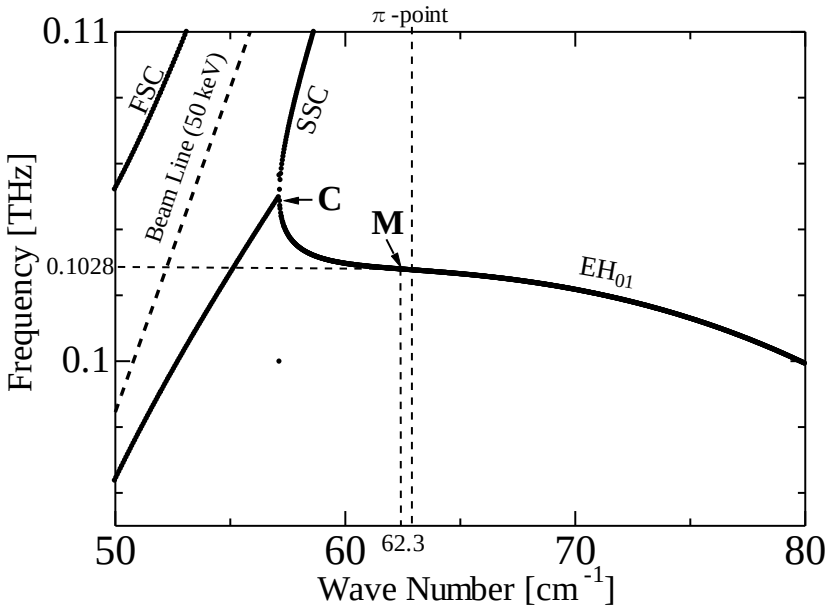

(b)

Fig. 4.3. Dispersion curves of axisymmetric mode (m = 0) with the beam radius R_b = 14.7 mm, the external magnetic field B_0 = 5 T, and the beam energy (a) 32.5 keV, and (b) 50 keV. Structure mode is hybrid transverse magnetic (EH_{01}) mode. Beam modes are fast space charge (FSC) and slow space charge (SSC) modes. As a reference, beam lines are also plotted. Point *C* gives the highest frequency of the unstable region for the beam mode. See Fig. 4.5 for point *M*. (Reproduced from Ref. [10])

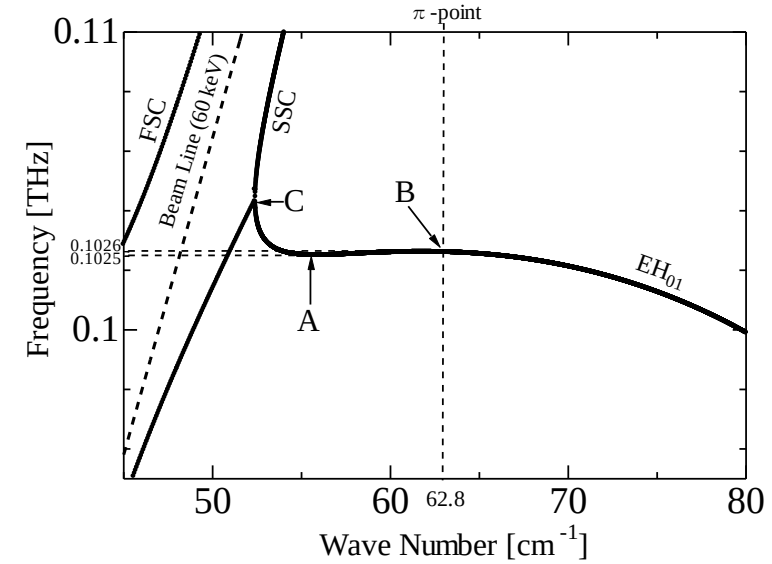

(a)

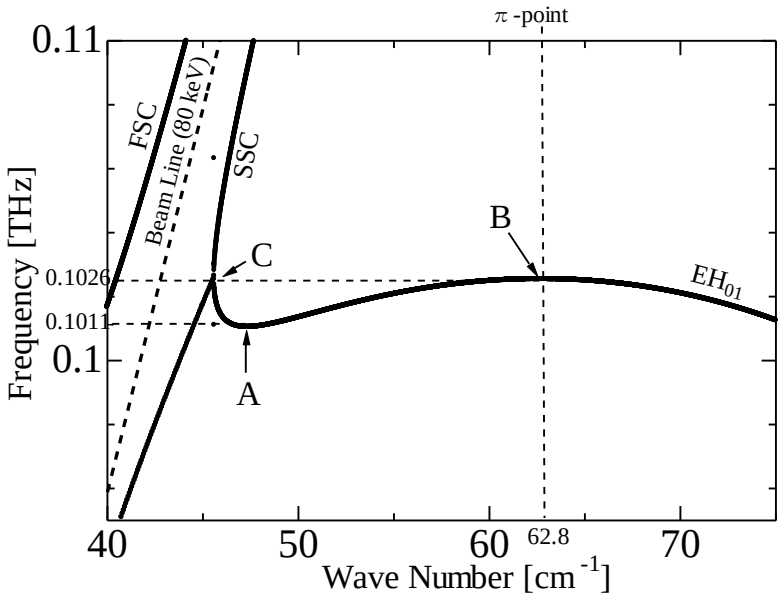

(b)

Fig. 4.4 Dispersion curves of axisymmetric mode (m = 0) with the beam radius R_b = 14.7 mm, the external magnetic field B_0 = 5 T, and the beam energy (a) 60 keV, and (b) 80 keV. Structure mode is hybrid transverse magnetic (EH_{01}) mode. Beam modes are fast space charge (FSC) and slow space charge (SSC) modes. As a reference, beam lines are also plotted. Point *C* gives the highest frequency of the unstable region for the beam mode. Points *A* and *B*; a double root formed by the SSC and forward-EH_{01} modes, and by the forward- and backward-EH_{01} modes. (Reproduced from Ref. [10])

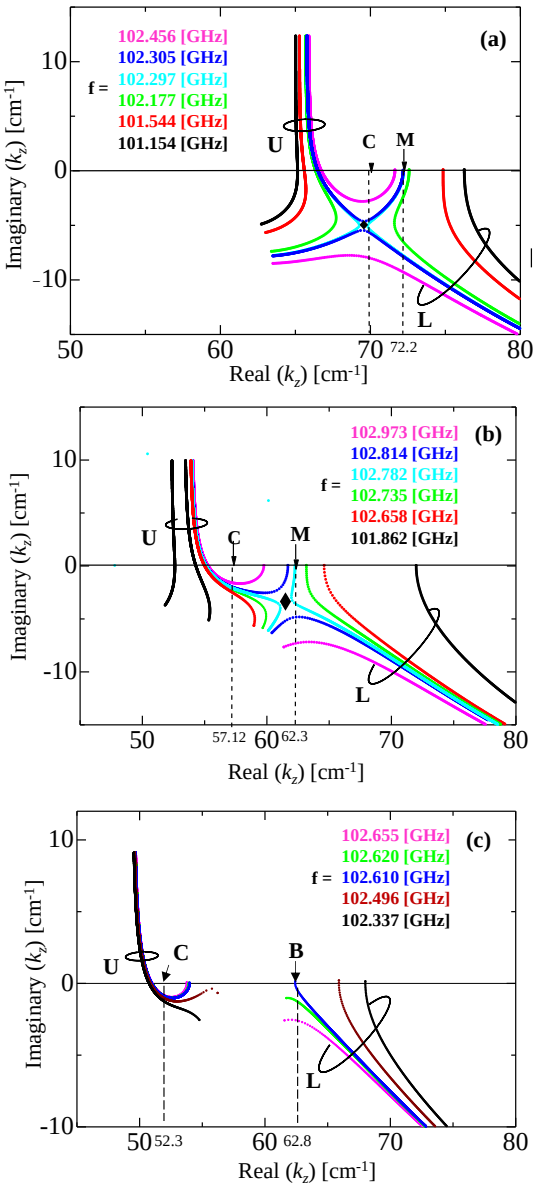

Fig. 4.5 Trajectory of roots in the complex wave number plane for the Cherenkov instability at the external magnetic field B_0 = 5 T. The beam energies are of (a) 32.5 keV, (b) 50 keV, and (c) 60 keV. Solid lines are obtained with constant ω_r by changing ω_i. Space charge modes and backward structure modes are denoted by *U* and *L*, respectively. A black diamond is a saddle-point. Point *C* gives the highest frequency of the unstable region for the beam mode. Point *M* in (a) and (b) separates the backward-EH_{01} mode and SSC mode on the imaginary (k_z) zero line. Points *A* and *B* in (c) correspond to points *A* and *B* in Fig. 4.4. (Reproduced from Ref. [10])

References

[1] R. J. Briggs, *Electron-Stream Interaction with Plasmas*. Cambridge, MA: MIT Press, 1964, ch 2.

[2] W. Liu, Y. Lu, L. Wang, and Q. Jia, "A multimode terahertz-Orotron with the special Smith-Purcell radiation," Appl. Phys. Lett. 108, 183510 (May 2016).

[3] O. Watanabe, K. Ogura, T. Cho, and Md. R. Amin, "Self-consistent linear analysis of slow cyclotron and Cherenkov instabilities," Phys. Rev. E, vol. 63, 056503, Apr. 2001.

[4] Y. Takashima, K. Ogura, M. Yamakawa, K. Otubo, and Md. R. Amin, "Analysis of slow-wave instability in rectangularly corrugated cylindrical waveguide," J. Plasma Fusion Res. SERIES, vol. 8, pp. 1512-1517, 2009.

[5] H. Yamazaki, O. Watanabe, Y. Yamashita, M. Iwai, Y. Suzuki, and K. Ogura, "Cherenkov and slow cyclotron instability in periodically corrugated cylindrical waveguide with low magnetic field region," IEEJ Trans. FM, vol. 124, no. 6, pp. 477-482, 2004.

[6] K. Ogura, A. Shirai, M. Ogata, S. Gong, and K. Yambe, "Beam interactions with surface waves and higher order modes in oversized G-band slow-wave structure," IEEE Trans. Plasma Sci., vol. 44, no. 2, pp. 201-210, Feb. 2016.

[7] K. Minami, Y. Choyal, and V. L. Granatstein, "Saddle-point analysis of a high-power backward-wave oscillator near Cyclotron absorption," IEEE Trans. Plasma Sci., vol. 32, no. 3, pp. 1100-1108, Jun. 2004.

[8] S. Gong, K. Ogura, K. Yambe, S. Nomizu, A. Shirai, K. Yamazaki, J. Kawamura, T. Miura, S. Takanashi, and M. T. San, "Experimental study of intense radiation in terahertz region based on cylinderical surface wave resonator," J. Appl. Phys., Vol. 118, 123101, Sep. 2015.

[9] J. T. Donohue, and J. Gardelle, “Simulation of Smith-Purcell terahertz radiation using a Particle-in-Cell code,” Phys. Rev. ST Accel. Beams, vol. 9, 060701, Jun. 2006.

[10] M. T. San, K. Ogura, K. Yambe, Y. Annaka, and J. Fujita, “Study on Operation of a Surface-wave Oscillator around the π point Region,” IEEE Trans. Plasma Sci., vol. 45, no. 1, pp. 30-38, Jan. 2017.

Chapter 5

Oscillation Starting Conditions of Surface-wave Resonators

5.1 Introduction

Two starting conditions: starting energy and starting current, can be theoretically predicted for intense radiation of BWOs. The starting current condition has been studied for the conventional BWO, and the starting energy condition for the oversized BWOs. The starting current of the BWO has been analyzed in [1], [2], and theoretical work for both conditions has been studied in [3]. The existence of the starting energy for the oversized K- and G-band BWOs has been experimentally and numerically pointed out in [4], [5]. For the oversized BWO, the starting energy becomes more critical than the starting current condition.

In Section 5.2, the dispersion relations of SWRs are presented. The SWRs (0.35 THz) and (0.5 THz) are recognized as the resonators and the interaction width Δk_z for both types are described by the temporal growth rate and saddle-point analysis. In Section 5.3, the numerical study of oscillation starting conditions: starting energy and starting current, are presented. In Section 5.4, the numerical and experimental results are analyzed for the oscillation starting conditions of the SWR (0.35 THz). In Section 5.5, the oscillation starting conditions of the SWR (0.5 THz) are presented by the numerical and experimental results. Summary and conclusion are presented in Section 5.6.

5.2 Dispersion Relation of Surface-wave Resonator

The dispersion relations of the SWRs (0.35 THz) and (0.5 THz) are physically similar to that of a surface-wave resonator presented in Section 4.2, and both types can be recognized as surface-wave resonators (SWRs). Different beam lines intersect the dispersion curve at different frequency range, and broadband radiation can be expected by a SWR. The upper cutoff frequency and group velocity of the electromagnetic wave are dramatically increased by decreasing *h*. Dispersion curves related to the group velocity of both types are shown in Fig. 5.1. The SWR (0.35 THz) has relatively slow group velocity compared with the SWR (0.5 THz). The group velocity of the SWR (0.5 THz) approaches to the velocity of light by some k_z early than that of the SWR (0.35 THz). And a beam line intersects two curves at different frequency region and wave number: the frequency and wave number at the intersection point on the SWR (0.35 THz) is lower than that of the SWR (0.5 THz). For the reasons, starting energy, which is presented in Section 5.3, of the SWR (0.5 THz) may not be less than that of the SWR (0.35 THz).

A dispersion curve of the resonator can be divided by two regions based on the group velocity: Region-I where the group velocity is relatively lower than the velocity of light, and Region-II where the group velocity is close to the velocity of light, as shown in Fig. 5.1. In cylindrical surface wave (CSW), Bloch waves due to the periodic structure and Sommerfeld waves due to plasma of metal surface are mixed [6], [7]. Numerically and experimentally studies of dispersion characteristics of CSW by a cavity resonant method using vector network analyzer are presented in [8], [9]. In Region-I, the surface wave is by the surface corrugation and Bloch wave is dominant. And in Region-II, the surface corrugation does not effect on the surface wave and Sommerfeld wave is dominant. Region-I is called bounded surface-wave region and is formed near the upper cutoff frequency, and Region-II is called hybrid surface-wave region and formed away from the upper cutoff frequency. When the beam energy is sufficiently large, the intersection of the beam

line with the curve is in Region-I. When the beam energy is getting low, the intersection point approaches to the boundary of the region and into Region-II. By the low beam energy, the meaningful radiation operating in BWO region may disappear due to high group velocity around Region-II, but in Region-I TWT operation can be expected again as shown in Fig. 5.1(b) for a beam line of 20 keV.

In case of non-zero electron beam, space charge effects modify the dispersion curve and the waveguide mode becomes EH_{01}, which is presented in Section 4.3. For higher beam energy, the interaction of the electron beam and structure mode is of three-wave process including fast space charge (FSC), slow space charge (SSC) and EH_{01}. The instability is in the low current or Compton regime [10]. The instability transits to the high current or Raman regime when the beam energy is decreased. This transition can be understood with the normalization of the beam current as $\pi I_b / \beta_b \gamma_b^3 I_A$, where $\beta_b = v_b/c$, v_b is the beam velocity, c is the velocity of light, γ_b is the relativistic factor, and I_A is Alfven current of 17 kA. By decreasing the beam energy, $\beta_b \gamma_b^3$ decrease and the normalize current increases to the high current regime even if I_b does not changed. And the interaction becomes two-wave process of SSC and EH_{01}. The dispersion curve for the SWR (0.35 THz) with beam energies of 20, 40, and 80 keV, and the beam current I_b of 100 A is shown in Fig. 5.2. The interaction is of three-wave process for the beam energy of 80 keV, and two-wave process for 20 keV, as shown in Fig. 5.2(a). The interaction width Δk_z for both SWRs shown in Fig. 5.2(b) reflects the strength of the beam interaction. Δk_z is an increasing function of the electron beam energy and decreasing function of the group velocity when the interaction is in Region-I. Due to the relatively lower group velocity of the SWR (0.35 THz) than that of the SWR (0.5 THz), Δk_z of the SWR (0.35 THz) is larger than that of the oscillator (0.5 THz) for the same beam energy.

The numerical results of Δk_z for both types by the saddle-point analysis are shown in Figs. 5.3 and 5.4. The roots marked by *B* coming from the upper half of

k_z-plane are the SSC beam modes, and the roots marked by *S* coming from the lower half of k_z-plane are the backward-EH_{01} modes. The modes merged at the saddle-point which is depicted by a black diamond. Figure 5.3(a), (b), and (c) are for Δk_z of the SWR (0.35 THz) with the beam energy of 80, 50, and 30 keV, respectively. For 80 keV case, the saddle-point is in the negative Im(k_z) region like the relativistic X-band BWO and the weakly relativistic K-band BWO, in which the beam interaction with electromagnetic wave is so strong that high-power operations are possible. The saddle-point approaches to zero axis of Im(k_z) plane and Im(k_z) > 0 region when the beam energy is getting low. For the SWR (0.5 THz), all saddle-points for the beam energy of 30–90 keV are in the Im(k_z) > 0 region, shown in Fig. 5.4. The values Δk_z of are much smaller than that of the SWR (0.35 THz).

5.3 Oscillation Starting Conditions

Two threshold conditions for intense radiation are of starting energy and starting current. The main difference between them comes from the boundary condition at the upstream end of the SWS. Zero reflection at the output end of the SWS is assumed for the starting current, and a finite reflection is considered for the starting energy.

5.3.1 Oscillation Starting Energy

Beam mode and forward and backward electromagnetic modes are depicted in Fig. 5.5, where k_b, k_z^+, and k_z^- are the wave numbers of the beam mode, and forward and backward electromagnetic modes, respectively. The energy between the beam and electromagnetic wave will be converted via the beam mode of k_b and the backward electromagnetic mode of k_z^-. We focus on the interaction of k_b and k_z^-. With *L* infinite, k_b and k_z^- coincide and form the saddle-point of (2.6), at which the absolute instability may occur. But for a finite *L*, the waves are reflected at the beam

entrance and other end of the SWS, and the oscillation will occur not at the saddle-point. If the beam is injected into the finite length SWS, the beam mode with k_b is excited and reflected with R_2 at the output end. The reflected wave is the backward surface wave with k_z^- propagates backward to the beam entrance, and reflected with R_1 at the beam entrance. The reflection coefficients of R_1 and R_2 affect the radiation [11]. The beam interaction can be expressed by the following equations presented in [2], [3].

$$D(f, k_b) = 0 \tag{5.1}$$

$$D(f, k_z^-) = 0 \tag{5.2}$$

$$R \exp\left\{-i\left(k_z^- - k_b\right)\right\} = 1. \tag{5.3}$$

Here, the beam mode, $R = R_1 R_2$ is one round-trip reflection coefficient of wave fields at both ends of the SWS, and for simplicity it is replaced by a real number $0 < R < 1$. The instability of the beam interaction for the finite L satisfying (5.1)-(5.3) is referred to as a global instability [11]. Equation (5.3) comes from the requirement that the field must be a single value at any axial position after one round-trip of the field, and is decomposed to the real and imaginary parts as

$$\mathrm{Re}\left(k_z^- - k_b\right) = -2\pi N / L > 0 = \Delta k_z' \tag{5.4}$$

$$\mathrm{Im}\left(k_z^- - k_b\right) = -\ln(R)/L > 0. \tag{5.5}$$

Here, N is an integer corresponding to the spatial harmonic of the periodic system. We limit to the dominant harmonic of N = -1. In order to satisfy (5.4), the interaction width Δk_z in the wave number space should be larger than $\Delta k_z'$, i.e.,

$$\Delta k_z \geq \Delta k_z'. \tag{5.6}$$

The numerically obtained Δk_z of both SWRs for EH_{01} mode is shown in Fig. 5.6 and 5.8. The interaction width Δk_z is an increasing function of the beam energy and

electron beam radius R_b. When R_b is increased, the gap between R_b and SWS inner wall G_b is decreased. And $\Delta k_z'$ is a decreasing function of the length of the SWS. In the figures, the beam energy at the point where the line with a given G_b crosses the $2\pi/L$ line is of the starting energy for the given length of the SWS. The longer the length of the SWS and/or the smaller G_b is, the lower the starting energy is. The starting energy is the minimum energy needed to operate based on a SWR, and beyond the energy the intense radiations appear.

5.3.2 Oscillation Starting Current

It should be noted that the oscillation satisfying (5.3) is based on a multi-reflection process like the laser or maser operation, which results in a strong radiation may be possible. As for the starting current, the different boundary conditions have been applied in [1]. The beam interaction is assumed to be the three-wave process approximated by the following equation,

$$\left(\delta\omega - v_b \delta k_z\right)^2 \left(\delta\omega - v_g \delta k_z\right) = \delta \tag{5.7}$$

and $\delta = a^3 I_b$. Here, $\delta\omega = \omega - \omega_0$ and $\delta k_z = k_z - k_{z0}$ are the modified angular frequency and wave number from ω_0 and k_{z0} with zero beam current. And v_g is the group velocity, and a is defined for a specific set of beam and SWS parameters [1], [12], [13]. Three boundary conditions must be satisfied in addition to the dispersion relation. The first two come from the requirement that the beam density and velocity perturbations vanish at the upstream end of the structure. The third condition is that there is no input field at the downstream end. This condition means no reflection at the output end of the structure and differs from the condition (5.3) based on the multi-reflection process. Considering these boundary conditions, solutions for the finite length case are obtained. And a threshold current exists, above which the imaginary part of $\delta\omega$ is positive. In [1], the normalized value of the stating current I_{bs} is obtained as

$$\left|\frac{a^3 I_{bs}}{v_b^2 v_g}\right| L^3 = 7.7. \tag{5.8}$$

It should be noted that v_g is less than v_b in the lower frequency case like the X-band BWO [1]. However, the opposite situation with v_g larger than v_b would happen in the terahertz oversized BWOs. This is caused by the broadband operation which includes the group velocity close to the light velocity in Fig. 5.1(c). Moreover, the beam interaction in the Raman regime as well as the Compton regime would be included as shown in Fig. 5.2(a).

5.4 Oscillation Starting Conditions of the SWR (0.35 THz)

In Fig. 5.6, the numerical and experimental results for the starting energy of the SWR (0.35 THz) are presented. The numerical values of Δk_z obtained from Section 5.2 are used in the figure. Δk_z is an increasing function of the beam energy and electron beam radius R_b. Dash lines represent $2\pi/L$ for various L, and the solid lines intersect each dash line. And numerically predicted starting energy can be assigned the beam energy at the intersection point of the solid and dash lines. The longer the length of the SWS is, the lower the starting energy occurs. The blue (black) sold lines with squares (circles) are for G_b of 0.075 mm (0.05 mm). When R_b is increased, G_b as well as the starting energy is decreased.

The experimental results plotted in the figure are obtained from Fig. 3.8, and represented by solid circles. The experimentally obtained starting energies are of 43, 35, and 22 kV when the length of the SWS of 60, 80, and $120z_0$. The experimental results show the starting energy of the SWR is also the decreasing function of the length of the SWS and has a good agreement with the numerical expectations. For the SWS of $40z_0$, meaningful radiation could not be generated by the beam voltage of up to approximately 90 kV. Therefore, the cathode diameter of 29.5 mm is used for the SWS of $40z_0$, and the starting energy of approximately 40

kV is obtained which is less than that of $60z_0$. And a remarkable agreement between the experimental and numerical results is on decreasing the starting energy by increasing R_b. The starting condition of the SWR can be explained by the starting energy and a SWR is formed by a global instability based on multi-reflection process.

The experimental results show the beam voltages as well as the corresponding beam currents at the oscillation starting conditions vary by the length of the SWS. The beam currents are of some hundred amperes. Numerically calculated starting currents by (5.8) for the SWR are shown in Fig. 5.7. The numerical ones are totally different from the experimental results. Therefore, the staring condition for the SWR could not be explained by the starting current condition of (5.8).

5.5 Oscillation Starting Conditions of the SWR (0.5 THz)

The numerical and experimental results for the starting energy of the SWR (0.5 THz) are shown in Fig. 5.8. The experimental values are obtained from Fig. 3.12. For the SWS of 120 and 160, the starting energy is approximately 75 and 40 kV, and the decreasing function of the length of the SWS. But increasing the length of the SWS to $320z_0$, the starting energy is approximately 35 kV which is slightly less than that of $160z_0$ and not as numerically expected value. And further increasing the SWS up to $400z_0$ could not reduce the starting energy anymore and the starting energy standstills at approximately 32 kV. Up to the SWS of $160z_0$, the resonator may be formed based on the round-trip of the electromagnetic field between the SWS ends and the starting condition given by (5.3) does work. The length of the SWS longer than $160z_0$ may be too long to form the resonator and the starting energy could not change from that of the SWS of $160z_0$.

Oscillation starting currents by the experimental results are of approximately 210, 8, 108, and 150 A for the SWS of 120, 160, 320, and $400z_0$, respectively. The numerical starting currents are shown in Fig. 5.9, and totally different from the experimental results. Therefore, oscillation starting condition for the SWR also could not be explained by the starting current condition of (5.8).

5.6 Summary and Conclusion

The saddle-point analysis results presented by green lines in Fig. 5.6 show that the value of Δk_z for the SWR (0.35 THz) does not increase and is nearly constant above 50 keV. Therefore, the SWS of $40z_0$ seems to be very marginal for satisfying the condition (5.6) with the cathode of 29 mm in diameter. By increasing the cathode diameter to 29.5 mm, the starting energy of short length SWS $40z_0$ is slightly less than that of $60z_0$ with the cathode diameter of 29 mm. When the beam energy is of less than 30 keV, the saddle-point moves into the region of $\mathrm{Im}(k_z) > 0$ as shown in Fig. 5.3. The interaction essentially is of two-wave process between the SSC and backward structure modes as mentioned referring to Fig. 5.2(a), and the same interaction width Δk_z can be obtained from Fig. 5.2(b) and 5.3(c). Although the unstable region becomes small, the interaction width Δk_z is wide enough to satisfy (5.6). By the dispersion relation shown in Fig. 5.1(a), the lowest starting energy of 23 kV for the SWR with the SWS of $120z_0$ is in Region-I, and further decreasing the beam line can be still in the region. Therefore, for the SWR (0.35 THz), the starting energy of less than 23 kV can be expected by the length of the SWS longer than $120z_0$.

For the SWR (0.5 THz) with the beam energy of from 90 to 30 keV, shown in Fig. 5.4, all saddle-points are located in the region of $\mathrm{Im}(k_z) > 0$. The values of Δk_z are much smaller than those of the SWR (0.35 THz) and become difficult to satisfy (5.6). For the relatively short length of 120 and $160z_0$, Δk_z can satisfy (5.6).

In other words, a surface-wave resonator is formed on the SWS surface of the SWR (0.5 THz). For the longer case of 320 or $400z_0$, the length may be too long to form such a long resonator. And hence, the starting energy does not decrease as expected. Fig. 5.8 shows that the longest length of the resonator may be around $160z_0$ with our experimental conditions. And by the dispersion relation shown in Fig. 5.1(b), the beam line of 32 keV intersects the dispersion curve where very close to the boundary of Region-I and Region-II. Further decreasing the beam line approaches to Region-II and coherence radiation could not be expected in the region. Therefore, for the SWR (0.5 THz) with relatively longer SWS could not be reduce the starting energy of less than approximately 32 kV.

For both SWRs, the oscillation starting condition could not be explained by the starting current condition. The oscillation starting current condition is dominant when the SWS is terminated in its characteristic impedance, which means no reflection from the output end of the SWS ($R_2 = 0$). However, in the experiment, characteristic impedance of the SWS may be mismatched with the structure impedance, and some reflection from the output end of the SWS may exit. Therefore, starting current condition is not dominant for the oscillation starting condition in the study.

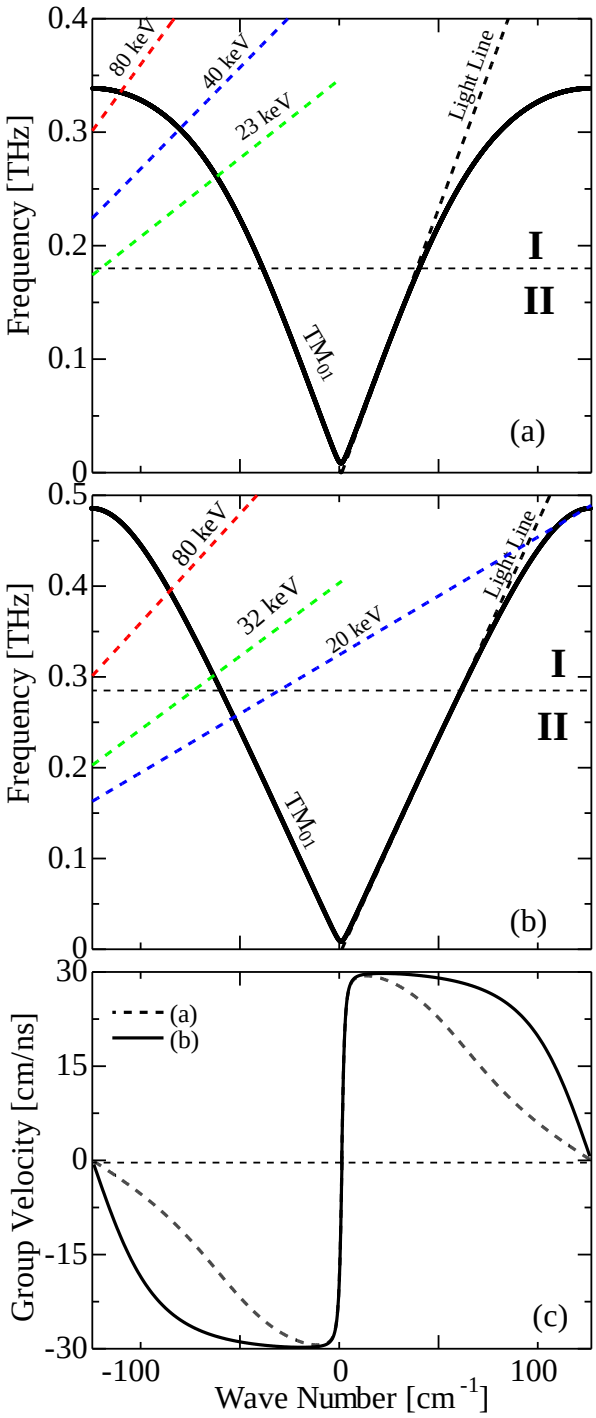

Fig. 5.1 Dispersion curves for (a) the SWR (0.35 THz), and (b) the SWR (0.5 THz). Dotted lines are of the light line and beams lines. (c) Group velocity of the electromagnetic wave for both SWRs.

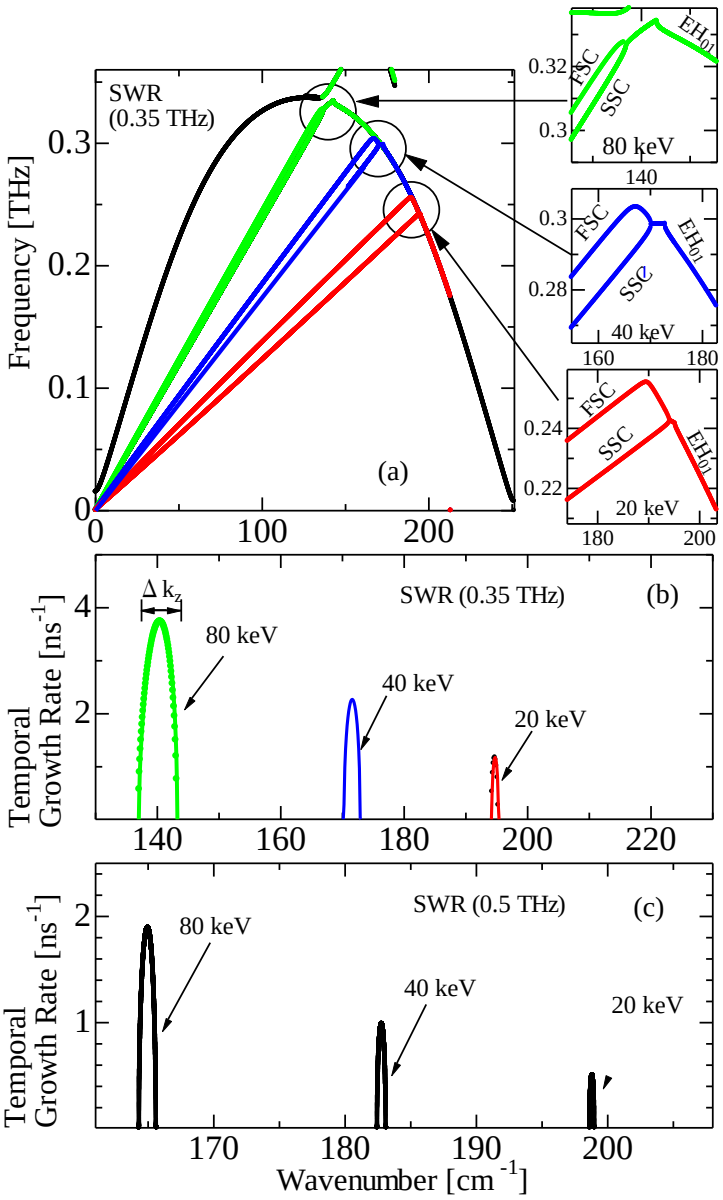

Fig. 5.2(a) Real parts of complex frequency vs real wave number for the SWR (0.35 THz) in the case of beam energies of 20, 40, and 80 keV. Fast space charge mode, slow space charge mode, and waveguide hybrid mode are denoted by FSC, SSC, and EH_{01}, respectively. Imaginary parts of complex frequency as a function of real wave number for (b) the SWR (0.35 THz) and (c) the SWR (0.5 THz) in the case of beam energies of 20, 40, and 80 keV. Δk_z is the interaction width. The gap between R_b and the SWS inner wall G_b is of 0.075 mm. (Reproduced from Ref. [14])

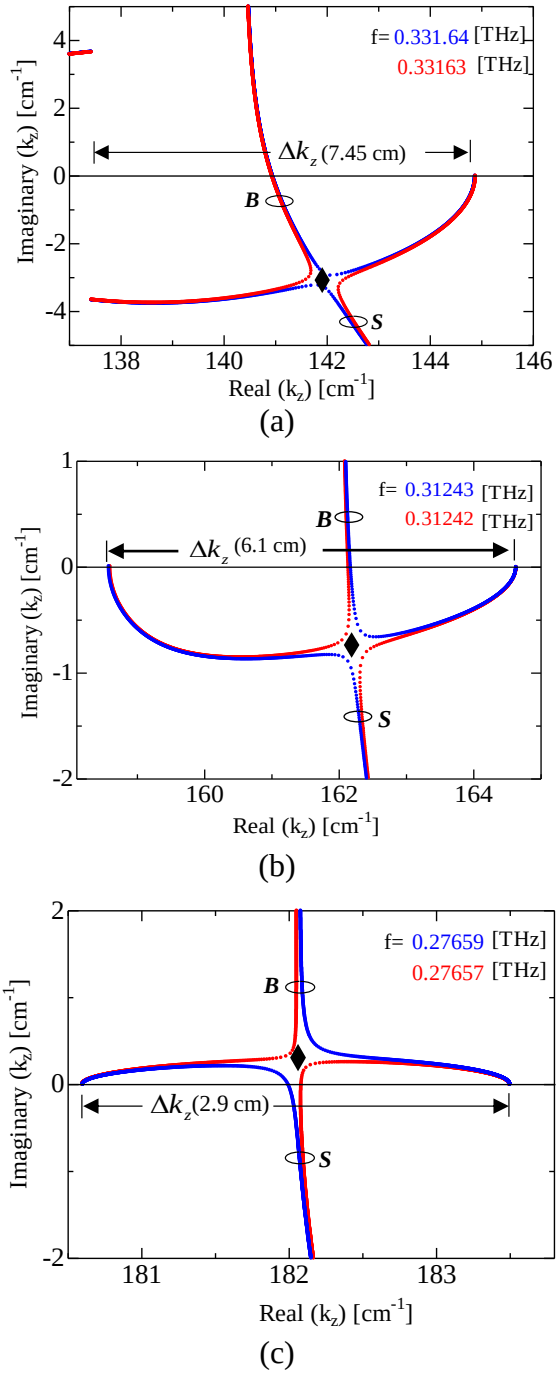

Fig. 5.3. Saddle-point analysis results of the SWR (0.35 THz) for beam energies of (a) 80 keV, (b) 50 keV, and (c) 30 keV. Slow space charge (SSC) beam modes and backward structure (EH_{01}) modes are denoted by *B* and *S*, respectively. A black diamond is of a saddle-point. Δk_z is of the interaction width.

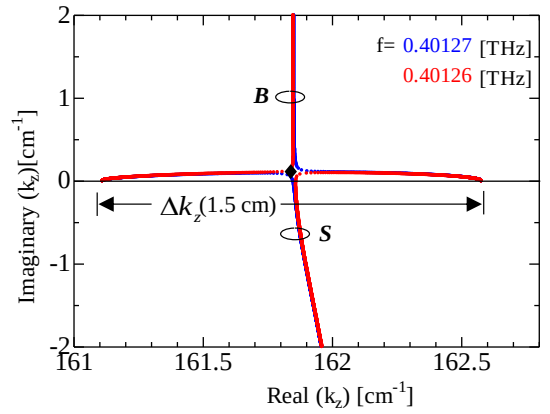

(a)

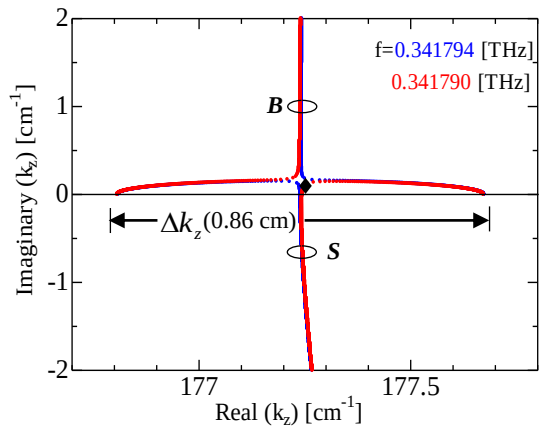

(b)

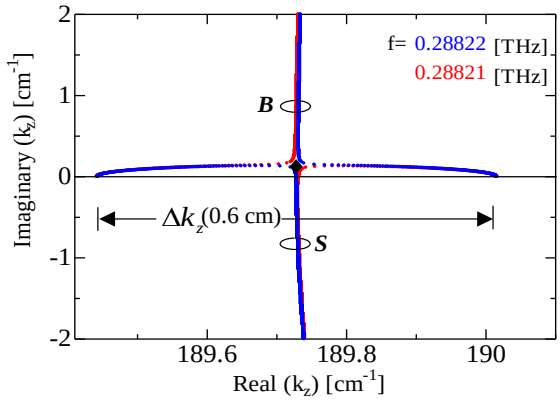

(c)

Fig. 5.4. Saddle-point analysis results of the SWR (0.5 THz) for beam energies of (a) 90 keV, (b) 50 keV, and (c) 30 keV. Slow space charge (SSC) beam modes and backward structure (EH_{01}) modes are denoted by *B* and *S*, respectively. A black diamond is of a saddle-point. Δk_z is of the interaction width.

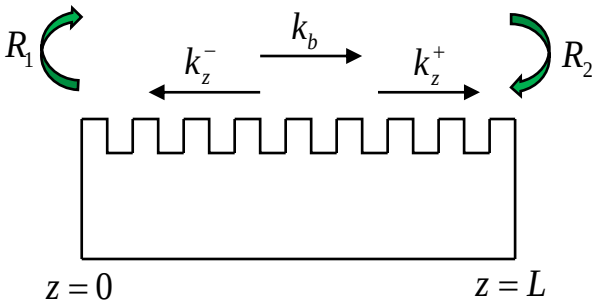

(a)

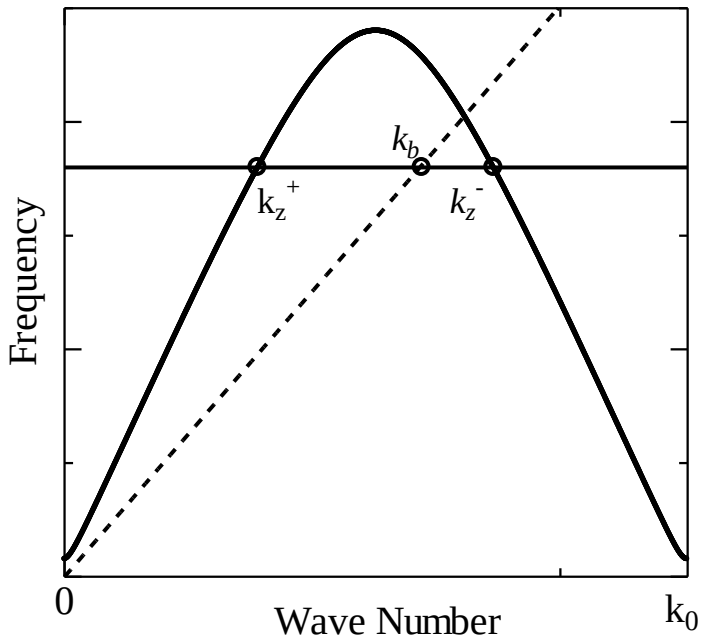

(b)

Fig. 5.5 Beam mode and forward and backward electromagnetic modes are represented by their wave numbers k_b, k_z^+, and k_z^-, respectively. Reflection coefficients at both end of the SWS are denoted by R_1 and R_2, respectively. (a) Waves coupling at the ends of $z = 0$ and $z = L$. (b) Schematic diagram for the width of global instability $\Delta k_z' = k_b - k_z^-$.

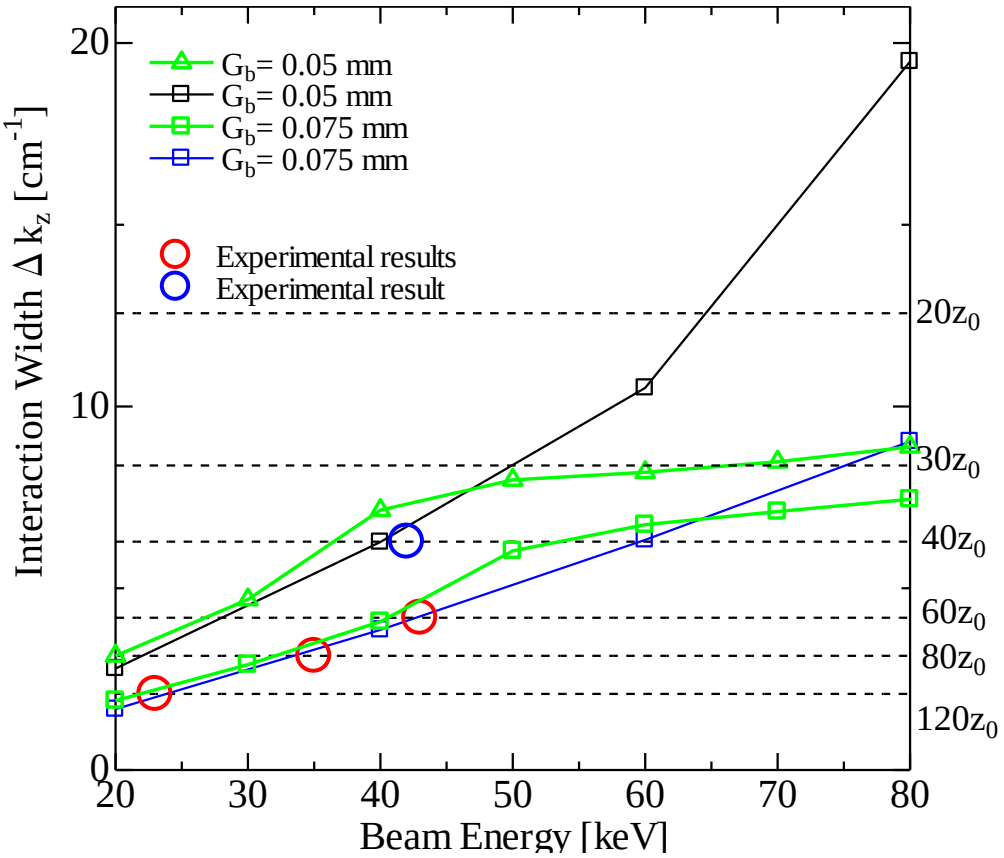

Fig. 5.6 Interaction width Δk_z and length of SWS L versus beam energy for G_b, the gap between R_b and the SWS inner wall, of 0.05, and 0.075 mm for the SWR (0.35 THz). Dash lines represent $2\pi/L$ for various L. Experimentally obtained starting energies using the cathode with diameter of 29 mm (red circles) and 29.5 mm (blue circle) are also plotted. Green lines are of the saddle-point analysis results. (Reproduced from Ref. [14])

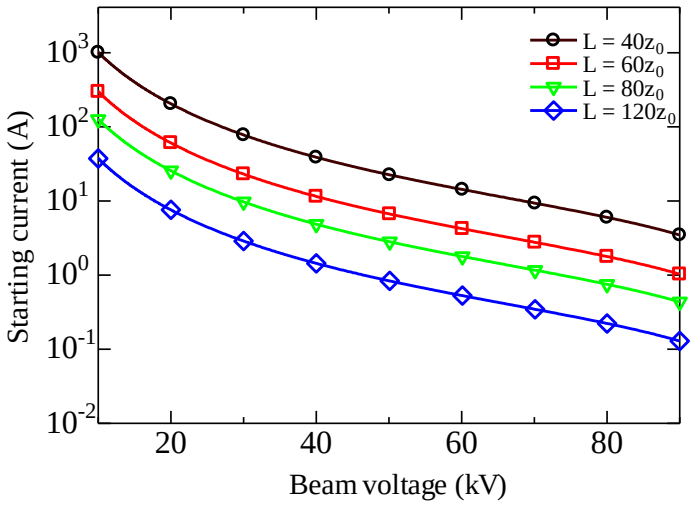

(a)

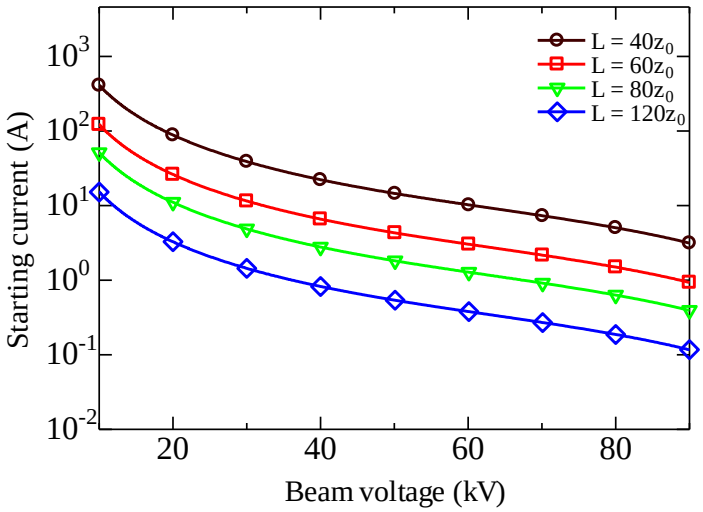

(b)

Fig. 5.7 Starting current of the SWR (0.35 THz) for (a) G_b = 0.075 mm, and (b) G_b = 0.05 mm.

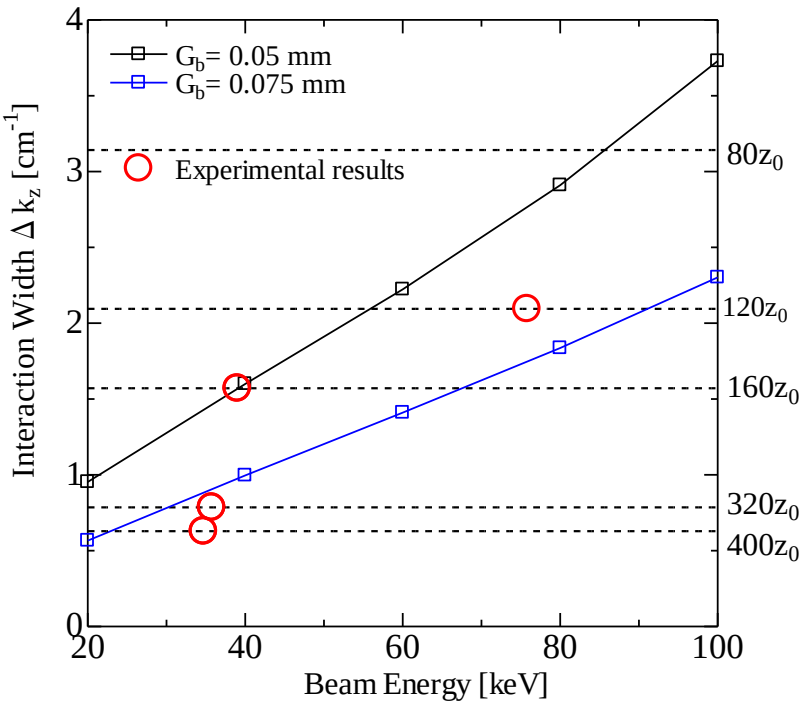

Fig. 5.8 Interaction width Δk_z and length of SWS L versus beam energy for G_b, the gap between R_b and the SWS inner wall, of 0.05, and 0.075 mm for the SWR (0.5 THz). Dash lines represent $2\pi/L$ for various L. Experimentally obtained starting energies using the cathode with diameter of 29 mm (red circles) are also plotted. Results by the saddle-point analysis and the temporal growth rate values are nearly in phase. (Reproduced from Ref. [14])

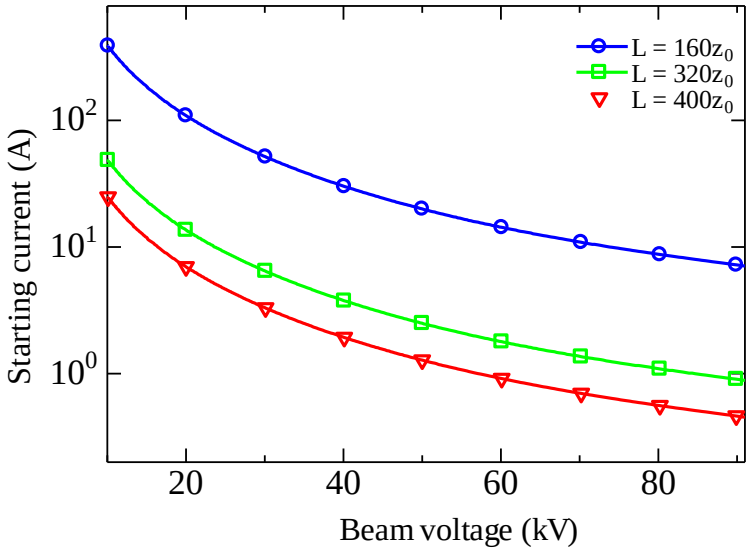

(a)

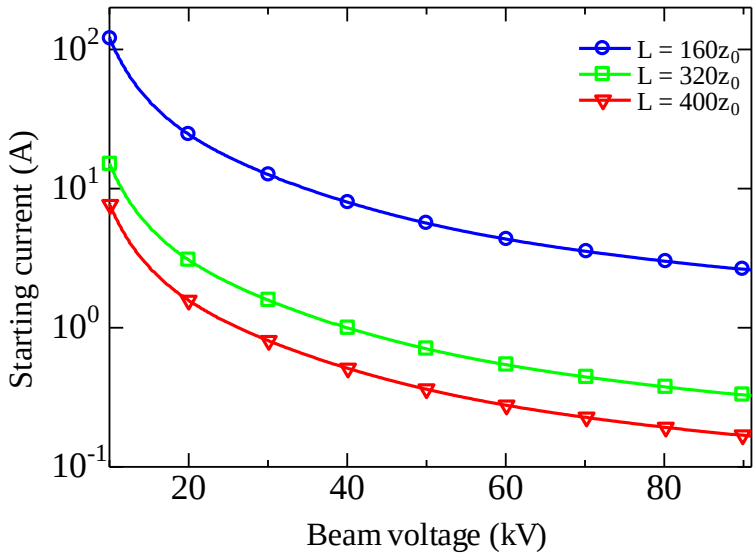

(b)

Fig. 5.9 Starting current of the SWR (0.5 THz) for (a) G_b = 0.075 mm, and (b) G_b = 0.05 mm.

References

[1] J. A. Swegle, “Starting conditions for relativistic backward wave oscillators at low currents,” Phys. Fluids, vol. 30, no. 4, pp. 1201-1211, Apr. 1987.

[2] K. Minami, M. M. Ali, K. Ogura, W. Kim, and T. Watanabe, “Analysis of starting currents in a backward wave oscillator with finite structure length,” J. Phys. Soc. Jpn., vol. 61, no. 10, pp. 3566-3575, Oct. 1992.

[3] K. Minami, K. Ogura, M. R. Amin, X. D. Zheng, T. Watanabe, Y. Carmel, W. W. Destler, and V. L. Granatstein, “Starting energy and current for a large diameter finite length backward wave oscillator operated at the fundamental mode,” IEEE Trans. Plasma Sci., vol. 23, no. 2, pp. 124-132, Apr. 1995.

[4] K. Ogura, R. Yoshida, Y. Yamashita, H. Yamazaki, K. Komiyama, and M. Sakai, “Study on oscillation starting condition of K-band oversized backward wave oscillator driven by a weakly relativistic electron beam,” J. Plasma Fusion Res. Ser., vol. 6, pp. 703-706, Mar. 2004.

[5] S. Gong, K. Ogura, S. Nomizu, A. Shirai, K. Yamazaki, K. Yambe, S. Kubo, T. Shimozuma, S. Kobayashi, and K. Okada, “Oscillation starting conditions for oversized G-band (140 – 220 GHz) backward wave oscillator driven by weakly relativistic electron beam,” IEEE Trans. Plasma Sci., vol. 43, no. 10, pp. 3530-3536, Oct. 2015.

[6] H. M. Barlow and A. L. Cullen, “Surface waves,” Radio Section, vol. 22, pp. 329, 1953.

[7] R. Porter and D. V. Evans, “Rayleigh–Bloch surface waves along periodic gratings and their connection with trapped modes in waveguides,” Fluid Mech., vol. 386, pp. 233-258, May 1999.

[8] K. Yamazaki, J. Kojima, A. Kojima, A. Shirai, K. Ogura, and K. Yambe, “Propagation characteristics of cylindrical surface waves on periodically corrugated metal,” Plasma conference 2014, 18PB-024.

[9] K. Ogura, H. Iiduka, and K. Yambe, “Cylindrical surface wave on periodically corrugated metal,” Plasma Fusion Res., vol. 7, pp. 2406022-1-4, Feb. 2012.

[10] J. A. Swegle, “Approximate treatment near resonance of backward and traveling wave tubes in the Compton regime,” Phys. Fluids, vol. 28, no. 12, pp. 3696-3702, Dec. 1985.

[11] E. M. Lifshitz, and L. P. Pitaevskii, Physical Kinetics, New York: Pergamon Press, 1981, pp. 281-283.

[12] S. Gong, K. Ogura, K. Yambe, S. Nomizu, A. Shirai, K. Yamazaki, J. Kawamura, T. Miura, S. Takanashi, and M. T. San, “Experimental study of intense radiation in terahertz region based on cylindrical surface wave resonator,” J. Appl. Phys. 118, no. 12, p. 123101, Sep. 2015.

[13] V. Kumar, and K. J. Kim, “Analysis of Smith-Purcell free-electron lasers,” Phys. Rev. E 73, p. 026501, Feb. 2006.

[14] M. T. San, K. Ogura, K. Kubota, Y. Annaka, K. Yambe, and A. Sugawara, “Study on Operation of Oversized Backward Wave Oscillator for Broadband Terahertz Radiation,” IEEE Trans. Plasma Sci., accepted for publication on Jan 11, 2018.

Chapter 6

Summary

BWO has been experimentally and numerically studied as SWO and SWRs for terahertz radiations. Radiated power of some kW is obtained by the beam energy with less than 80 kV. Peak radiating frequency is of 0.1 THz by the SWO, 0.35 and 0.4 THz by SWRs. The SWO (0.1 THz) operates as a surface-wave oscillator. With long length of the SWS, the SWO operates in BWO and TWT regions, and not at the π-point region. With relatively short length of the SWS, the SWO operates in all regions: BWO, π-point, and TWT regions. Operating frequency is a single value around 0.1 THz and not tuneable. The SWR (0.35 THz) operates as a surface-wave resonator, and operating frequency range is of 0.26–0.34 THz. The SWR (0.5 THz) also operates as a surface-wave resonator with radiation frequency range of 0.31–0.4 THz. Both SWRs have broadband radiation of 0.1 THz which is tuneable adjusting the electron beam voltage of less than 80 kV.

By the numerical studies of real wave number analysis and saddle-point analysis, the operation of the SWO (0.1 THz) is recognized. In BWO and TWT regions, the Cherenkov interaction is absolute and convective instability, respectively, and around the π-point region, the instability is of absolute instability.

Oscillation starting conditions of the SWRs (0.35 THz) and (0.5 THz) are could not be explained by the starting current condition. The starting energy of the SWR (0.35 THz) is decreased when the length of the SWS and/or the cathode

diameter is increased. The experimental results coincide with numerical predictions for the starting energy of the SWR. Therefore, the oscillation starting condition of the SWR can be explained by the starting energy. The starting energy of the SWR (0.5 THz) is also reduced increasing the length of the SWS. But for relatively long length of the SWS, the starting energy could not be decreased anymore.

In conclusion, three types of SWSs with different corrugation amplitudes have been studied. The SWO (0.1 THz) with deeper corrugation amplitude has lower group velocity of electromagnetic wave and radiated power is more intense than other. With relatively low corrugation amplitude, the SWRs (0.35 THz) and (0.5 THz) have fairly high group velocity, and radiation frequency is tunable varying the electron beam voltage. Oscillations around the π-point region of the SWO are experimentally pointed out, and numerically explained that the instability at π-point operation is of absolute instability. Broadband radiation frequency is obtained by the SWRs, and the starting energy could not be a decreasing function of the length of the SWS when the resonator with relatively low corrugation amplitude is used.

List of Publications

1. M. T. San, K. Ogura, K. Yambe, Y. Annaka, S. Gong, J. Kawamura, T. Miura, S. Kubo, T. Shimozuma, S. Kobayashi, and K. Okada, “Experimental study on W-band (75 – 110 GHz) oversized surface wave oscillator driven by weakly relativistic electron beams,” Plasma Fusion Res., vol. 11, p. 2406085, Jun. 2016.

2. M. T. San, K. Ogura, K. Yambe, Y. Annaka, and J. Fujita, “Study on Operation of a Surface-wave Oscillator around the π point Region,” IEEE Trans. Plasma Sci., vol. 45, no. 1, pp. 30-38, Jan. 2017.

3. M. T. San, K. Ogura, K. Kubota, Y. Annaka, K. Yambe, and A. Sugawara, “Study on Operation of Oversized Backward Wave Oscillator for Broadband Terahertz Radiation,” IEEE Trans. Plasma Sci., vol. PP, no. 99, pp. 1-9 (tentative), Feb. 05, 2018 published (Early access).